Engineering Fracture Mechanics 345 (2026) 112504

Contents lists available at ScienceDirect

Engineering Fracture Mechanics

journal homepage: www.elsevier.com/locate/engfracmech

Modeling interlayer interfaces in 3D-printed concrete using a coupled cohesive contact approach

Gianluca Mazzucco *, Massimiliano Maletta, Riccardo Lando, Jiangkun Zhang, Valentina Salomoni, Beatrice Pomaro

Department of Civil, Environmental and Architectural Engineering, University of Padua, Via Marzolo 9, 35131 Padova, Italy

ARTICLE INFO

Keywords:
Finite element method
Contact mechanics
3D-printed concrete
Cohesive model

ABSTRACT

3D-printed concrete exhibits pronounced anisotropy as a result of its layered deposition process and the presence of interfacial contact zones, which significantly influence its mechanical response. This work presents a Finite Element framework enhanced with contact mechanics to explicitly model the interaction between adjacent printed layers. A cohesive contact formulation is adopted to describe the evolution of normal and tangential stresses at the interfaces. The model incorporates coupled normal and tangential traction–separation laws, enabling the representation of elastic, inelastic, and residual interfacial behavior. The elasto-plastic evolution of the interface response is governed by a quadratic failure criterion, with hardening/softening functions calibrated from direct tensile and shear tests. The numerical implementation relies on a classical return-mapping algorithm to ensure a consistent update of interfacial stresses and inelastic displacement components.

The proposed model is validated against experimental data for three different materials through case studies involving direct tension, shear, compression, and four-point bending tests. The results demonstrate that the cohesive contact formulation accurately captures the role of interfacial properties in governing macroscopic strength, failure mechanisms, and anisotropic behavior.

Specifically, the proposed model is capable of reproducing post-peak softening through calibrated hardening/softening laws. Experimental validation of this constitutive behavior is provided for the case studies with complete force–CMOD measurements, whereas the remaining cases validate primarily the peak response and the associated failure mechanisms.

1. Introduction

Three-dimensional printed concrete (3DPC) is a rapidly developing technology in the construction sector, particularly as a more environmentally friendly alternative. Portland cement production accounts for nearly 10% of global CO_2 emissions [1], making the optimization of production and construction processes critically important. 3DPC addresses these challenges by reducing construction time, minimizing material waste and production costs, automating construction processes, and improving safety [2]. 3DPC is manufactured through the successive deposition of extruded filament layers, during which interlayer contact interfaces are formed and govern the anisotropic mechanical behavior of the material. Interlayer adhesion is strongly influenced by printing parameters such as the time interval between layer depositions, nozzle speed, and nozzle height [3]. In addition, voids may accumulate between layers, adversely affecting cohesion as well as compressive and flexural strengths [4].

* Corresponding author.
E-mail address: mazzucco.gianluca@unipd.it (G. Mazzucco).

https://doi.org/10.1016/j.engfracmech.2026.112504
Received 13 May 2026; Received in revised form 13 July 2026; Accepted 28 July 2026

Available online 4 August 2026
0013-7944/

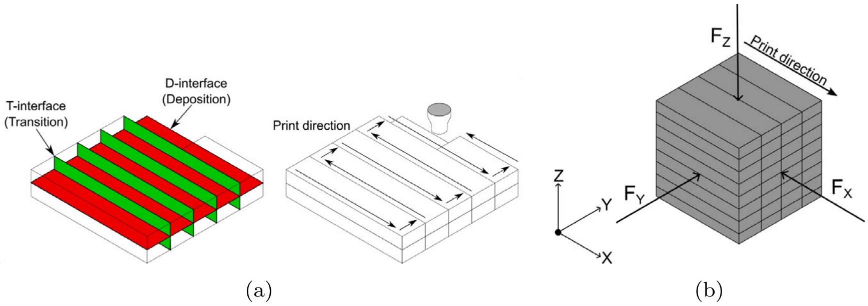

Fig. 1. Deposition and transition interfaces in 3D printing (a). Main loading directions in 3DPC: X or D1, Y or D2, Z or D3 (b).

Recently, these phenomena have been investigated using Finite Element (FE) methods, in which cohesive elements are explicitly introduced at the interlayer interfaces and assigned contact properties [5–8]. The macroscopic behavior of 3DPC is then evaluated as a function of these properties, either through comparison between numerical predictions and experimental data or via parametric studies. In the previously cited studies, a bilinear traction–separation law is typically assumed [9], in which both normal and tangential strengths increase to a peak value and subsequently degrade to zero residual strength. The presence of multiple layers and interlayer separation interfaces makes 3DPC an anisotropic material. Two types of interfaces typically develop during 3D concrete printing, as illustrated in Fig. 1(a). The first, commonly referred to as the *Deposition interface* (D-interface), forms between successive printed layers. The second, termed the *Transition interface* (T-interface), develops between adjacent filaments deposited side by side.

Accordingly, three principal loading directions are commonly considered and are defined with respect to the orientation of the printed layers, as illustrated in Fig. 1(b): the longitudinal direction (X), the transverse direction (Y), and the orthogonal direction (Z). The longitudinal, transverse, and orthogonal directions are also commonly denoted as D1, D2, and D3, respectively.

Large air voids may form between layers due to the absence of compaction during the printing process, leading to reduced interlayer adhesion and compromised mechanical strength [4]. Further, the lack of formwork promotes interstitial water evaporation, which may result in cracking [10].

Several studies have investigated the dependence of interlayer adhesion on printing parameters [3]. Common experimental configurations include compression tests, three- or four-point bending tests, direct tension tests, and shear tests. Specimens are typically obtained by sectioning larger printed elements to ensure consistent printing parameters [3,5,11,12]; alternatively, specimens may be printed individually [13,14].

The majority of existing studies on the mechanical characterization of 3DPC employ cubic specimens of varying dimensions due to the absence of standardized testing protocols. Consequently, literature data allow only general trends in compressive strength behavior along the three principal directions to be identified, as experimental campaigns often report inconsistent results. The primary consensus among studies is that the compressive strengths of 3DPC in all three directions are lower than those of conventionally cast concrete produced with the same mixture [15–19].

Several authors have reported that compressive strength is strongly influenced by the presence of voids, which is highly dependent on print quality and pumping pressure [20]. The extrusion of dense and cohesive filaments reduces porosity, thereby enhancing material strength. Most studies indicate that compressive strength is highest in the longitudinal direction (X), intermediate in the orthogonal direction (Z), and lowest in the transverse direction (Y) [14,15,17,19,21,22]. These differences have been attributed to variations in filament compaction, with higher extrusion pressures acting in the longitudinal direction and lower compaction occurring in the transverse direction due to lateral expansion in the absence of formwork [21,22]. However, other studies report contrasting trends, with the highest compressive strength observed in the orthogonal direction (Z) and the lowest in the longitudinal direction (X) [23–25].

Further, increasing the time interval between filament depositions has been shown to reduce compressive strength in all three directions [22]. The influence of nozzle geometry on compressive strength has also been reported [26].

Analogous to compressive strength, three principal loading directions are considered when evaluating the anisotropic bending response of 3DPC [10,16,17,21,24]. The orthogonal direction (Z) typically exhibits the highest crack resistance. Failure often initiates in the lower central zone, involving the outermost layers, where concrete tensile strength controls flexural behavior. Filament compaction is critical, as lower layers are more densely packed than upper layers, which can increase or decrease flexural strength. This effect is particularly relevant when specimens are extracted by mechanical cutting from larger printed elements. Additional factors enhancing Z-direction bending resistance include lower water-to-binder ratios in lower layers caused by bleeding.

In contrast, the longitudinal direction (X) is generally the weakest, correlating with interlayer bond strength. Tensile strength plays a decisive role in bending, and fiber reinforcement has been shown to significantly improve performance. For instance, the addition of 0.25%–1.0% of 3 mm-long glass fibers in a geopolymer mortar increased bending strength [21], while basalt fibers produced similar improvements [16]. Layer deposition time also affects bending behavior: longer intervals between successive layers reduce interlayer bond strength and, consequently, flexural performance, particularly in the X direction [17,22].

Tensile strength tests are also important for the characterization of 3DPC. Such tests between two filaments are used not only to determine overall strength but primarily to assess the influence of printing parameters on interfacial behavior. The two most commonly employed methods are the direct tensile test [3,10,11,22,27] and the Brazilian (tensile splitting) test [16,17,19].

In the absence of standardized protocols for 3DPC, specimen dimensions and geometries vary, and tests may be conducted on two filaments or on multilayer specimens. The Brazilian test is generally performed on cubic specimens.

The time interval between layer depositions has been identified as one of the most critical factors affecting interfacial tensile strength [3,10,17,22]. For example, [3] investigated tensile strength by superimposing two layers at time intervals of 5, 10, 15, and 20 min using the same mix, observing a gradual decrease in strength with increasing time. This effect was attributed to a thin surface film of fine aggregates, known as the lubrication layer, which is formed during pumping and gradually disappears, reducing adhesion.

A different behavior is reported by [22], who tested intervals of 10, 20, and 30 min. In this case, the 10- and 30-minute intervals yielded higher tensile strengths than the 20-minute interval. This behavior is explained by variations in surface moisture content: initially, the surface is highly moist due to the lubrication layer; over time, moisture decreases due to evaporation, but after a sufficiently long period (e.g., 30 min), bleeding increases surface moisture, enhancing interfacial strength.

Fiber addition has been found to have minimal or negligible effects on interfacial cohesion [28]. In some instances, tensile strength may even decrease, as fibers on the surface can promote void formation [24].

Shear tests are also employed for the mechanical characterization of 3DPC. Common methods include direct shear tests on single or double interfaces [18,28–30], inclined surface (slant-shear) tests [31], Iosipescu tests [8,32], and torsional shear tests [30,33,34].

Achieving a pure shear condition at an interface is challenging due to eccentricity effects of the applied load, which induce normal stresses. In 3DPC, shear stresses at separation surfaces are typically of limited significance, as layers are clearly distinct and interfaces consist primarily of a thin film of fine aggregates with minimal interlocking. Once tangential cohesion is exceeded, brittle failure occurs, making post-peak behavior difficult to capture; consequently, shear fracture energy is generally considered very small.

[32] correlated shear strength with different adhesives (epoxy, cementitious, and phosphate-based) used to join 3D-printed elements, considering four mechanical interlocking configurations: V-type, S-type, π-type, and I-type.

Innovative methods, such as torsional shear tests, show potential for generating approximately uniform shear stresses at the interface and for investigating combined shear and compressive effects [33,34].

Overall, interface tensile and shear strengths are typically 20%–30% lower than those of conventional concrete [18,28], although this range is indicative, as both properties are highly sensitive to printing parameters.

In recent years, several finite element (FE) approaches have been proposed to investigate the mechanical behavior of 3D-printed concrete by explicitly modeling the interlayer interfaces through cohesive elements or cohesive contact formulations. In most of these studies, the interface response is represented by bilinear traction–separation laws, in which the normal and tangential behaviors are treated independently and evolve according to uncoupled constitutive relationships. Although these approaches have proven effective for reproducing interface debonding under predominantly tensile or shear loading, they do not explicitly account for the interaction between normal and tangential stresses that naturally develops at interfaces subjected to mixed-mode loading. As a consequence, the influence of compressive or tensile normal stresses on the available shear resistance is generally neglected or only approximately represented through simplified constitutive assumptions.

In this work, a FE framework based on cohesive contact mechanics is developed to overcome these limitations. Unlike conventional cohesive formulations employing uncoupled bilinear traction–separation laws, the proposed interface model adopts a coupled elasto-plastic cohesive constitutive formulation in which the normal and tangential stress components evolve simultaneously through a quadratic failure criterion. Within this framework, the tangential strength depends explicitly on the current normal stress state, thereby naturally reproducing the interaction between interface opening, closure, sliding, and mixed-mode loading conditions. This coupling is particularly relevant for 3DPC, where interlayer interfaces are frequently subjected to combined normal and shear actions arising from bending, compression-induced lateral expansion, and complex multiaxial loading conditions.

The proposed cohesive contact formulation further extends the capabilities of existing interface models by allowing a complete description of the interface response throughout the loading process. The constitutive model explicitly accounts for interface opening, closure, tangential sliding, and their mutual interaction through the coupled failure criterion. The irreversible evolution of the interface is described by nonlinear hardening and softening laws in both the normal and tangential directions, which can be directly calibrated from experimental tensile and shear interface tests whenever such data are available. Moreover, the formulation allows the introduction of a residual tangential strength after damage initiation, enabling the representation of aggregate interlocking and friction-like mechanisms that may continue to transfer shear stresses even after significant interface degradation.

From a computational standpoint, the proposed methodology is implemented within the Abaqus [35] FE framework through a user-defined `UINTER` contact subroutine. Unlike approaches based on zero-thickness cohesive elements, the present implementation treats the interface directly as a contact interaction between adjacent printed layers. This strategy avoids the need for inserting cohesive elements into the finite element mesh, simplifies model generation for complex geometries, and provides greater flexibility for the simulation of interface opening, closure, and re-contact during nonlinear analyses.

The proposed model is validated through three independent experimental case studies involving different materials, printing configurations, and loading conditions, including direct tension, shear, compression, and four-point bending tests. In addition to reproducing peak strengths, the model accurately captures force–displacement and force–CMOD responses, post-peak softening, in those case studies for which complete experimental softening data are available, and the experimentally observed failure mechanisms.

The validation demonstrates that the coupled cohesive contact formulation provides a physically consistent description of interface degradation and significantly extends the applicability of interface modeling for 3D-printed concrete subjected to complex mixed-mode loading.

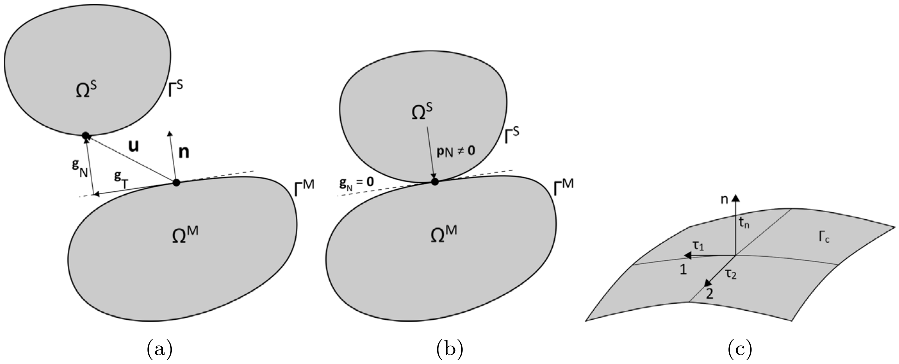

Fig. 2. Gap function (a). Contact condition (b). Stress on the contact surface (c).

Thus, the main objectives of this study are: (i) to develop a robust mechanical model capable of reproducing the material response through comparison with experimental data; (ii) to enable a macroscopic characterization of material anisotropy; and (iii) to accurately calibrate cohesive contact parameters for reliable simulation of interlayer behavior.

The paper is organized as follows: Section 2 presents the numerical methodology; Section 3 describes the experimental case studies and Section 4 discusses the numerical results in comparison with experimental data. Section 5 summarizes the main findings and conclusions.

2. Cohesive contact model for interface behavior

Numerical modeling of interlayer interfaces is based on the principles of the Cohesive Zone Model [36]. This approach employs cohesive traction–separation laws to describe the interaction between surfaces within the cohesive zone. In general, these laws relate the evolution of interfacial stresses to the separation distance, defining the elastic phase of the response and subsequent inelastic development.

This model is widely used in fracture mechanics to describe the formation and subsequent crack propagation in quasi-brittle materials under static and fatigue loading conditions, as well as in the study of bonded joints, contact zones between two dissimilar materials, fractures in metals and polymers.

The model is based on three fundamental hypotheses:

- A cohesive zone exists near the crack tip, consisting of two surfaces in contact that interact through cohesive forces.
- The fracture geometry and applied loads do not alter the distribution or magnitude of stress within the cohesive zone.
- Stress along the fracture is finite and continuously distributed, with no singularities at the crack tip.

Recent research has shown that the mechanical performance of 3DPC is strongly influenced by the properties of interlayer interfaces [37]. These interfaces, formed between successive deposited layers, act as preferential cracking zones where material separation and failure initiate. The high porosity observed in these zones significantly affects both strength parameters and elastic properties [4].

Specifically, to simulate the mechanical behavior of interlayer interfaces in 3DPC using FE methods a cohesive contact algorithm is developed. The model describes the interaction between surfaces through a traction–separation relationship, capturing both the initiation and propagation of cracks along the interface. Coupling between normal and tangential stress components is incorporated to account for the influence of multiaxial loading on interfacial response.

2.1. Contact model

The contact formulation between two bodies can be described as follows. Consider two bodies, M and S, in their initial configuration Ω^M and Ω^S (Fig. 2(a)), respectively. The two points on the respective surfaces Γ^M and Γ^S that are at minimum distance from each other are identified. Let $\mathbf{u}^M$ and $\mathbf{u}^S$ denote the displacement vectors of these surface points. The relative displacement between the two points is then defined as

$$\mathbf{u} = \mathbf{u}^S - \mathbf{u}^M \quad \text{on} \quad \Gamma = \Gamma^S \cup \Gamma^M. \tag{1}$$

Considering $\mathbf{n}$ as the normal to Γ^M, the normal and tangential components of the gap function $\mathbf{g}^T = \left[g_N, \mathbf{g_T}\right]$ are defined as

$$\begin{aligned} g_N &= \mathbf{u} \cdot \mathbf{n} \quad \text{on} \quad \Gamma \\ \mathbf{g_T} &= (\mathbf{I} - \mathbf{n} \otimes \mathbf{n})\mathbf{u} \quad \text{on} \quad \Gamma, \end{aligned} \tag{2}$$

where g_N represents the normal gap, $\mathbf{g_T}$ is the tangential gap between the two contacting surfaces and $\mathbf{I}$ is the identity tensor.

The non-penetration constraint is imposed on the normal gap function as: $g_N \geq 0$. When contact is open ($g_N > 0$), no normal force is transmitted ($p_N = 0$). When the two surfaces come into contact ($g_N = 0$), the normal force becomes active ($p_N < 0$). Once contact is established, a contact surface Γ_c can be defined as the intersection of the two surfaces: $\Gamma_c = \Gamma^S \cap \Gamma^M$ (Fig. 2(c)).

This formulation corresponds to the Hertz–Signorini–Moreau conditions for frictionless contact. In the context of optimization theory, these conditions are expressed as the Kuhn–Tucker–Karush conditions

$$g_N \geq 0, \quad p_N \leq 0, \quad p_N g_N = 0. \tag{3}$$

On the contact surface Γ_c, tangential forces $\mathbf{p}_T \neq 0$ may also develop. Defining the vector of forces acting on the contact surface as: $\mathbf{p}^T = [p_N, \mathbf{p}_T]$, the components of the relative stress along the three principal directions $[n, 1, 2]$ (1, 2 being two orthogonal tangential directions) are expressed as

$$\mathbf{t} = \lim_{\Gamma_c \to 0} \frac{\mathbf{p}}{\Gamma_c} = \begin{bmatrix} t_n \\ \tau_1 \\ \tau_2 \end{bmatrix}, \tag{4}$$

where $\mathbf{t}$ is the stress vector on the contact surface, which can also be expressed as: $\mathbf{t}^T = [t_n, \boldsymbol{\tau}^T]$, with $\boldsymbol{\tau}^T = [\tau_1, \tau_2]$, where t_n is the normal stress and $\boldsymbol{\tau}$ represents the tangential stress components (see Fig. 2(c)). The magnitude of the tangential stress is defined as: $\tau = \sqrt{\tau_1^2 + \tau_2^2}$.

2.2. Physical interpretation of the interface states

The proposed contact formulation distinguishes four different mechanical states of the interface, which naturally arise during the loading process. Initially, the interface behaves elastically while the relative displacements remain within the admissible domain defined by the cohesive law.

When the normal gap becomes positive, the interface progressively opens and transmits cohesive tensile stresses according to the traction–separation law. Once the accumulated inelastic normal displacement reaches the prescribed critical value, the interface is considered fully decohered and can no longer transmit tensile tractions.

Conversely, when the normal gap is zero or negative, the opposing surfaces remain in contact and compressive contact pressures may develop according to the contact constraints. Under these conditions, sliding between adjacent layers may still occur if the tangential stresses reach the interface failure criterion.

Tangential sliding is initiated when the coupled normal–tangential stress state reaches the quadratic failure surface. Beyond this point, irreversible tangential displacements develop according to the adopted plastic flow rule, while the interface strength evolves through the prescribed hardening or softening laws.

Finally, the proposed formulation naturally represents mixed-mode interface failure, in which opening and sliding simultaneously contribute to interface degradation through the coupled quadratic failure criterion. Such mixed-mode conditions are frequently encountered in 3DPC under bending, compression-induced lateral expansion, and other multiaxial loading configurations.

2.3. Cohesive law

The mechanical behavior of a contact pair is described using cohesive contact laws, which relate cohesive stresses to the relative displacement between the two points.

The gap function $\mathbf{g}$, which describes the relative displacement between the two points, can be additively decomposed to separate elastic and inelastic components, following the elasto-plastic formulation proposed by Wriggers and Laursen [38]

$$\mathbf{g} = \mathbf{g}^e + \mathbf{g}^s. \tag{5}$$

The first, elastic component $\mathbf{g}^e$, corresponds to the *stick condition*, in which the two bodies remain in contact and deformations are fully recoverable. The second, inelastic component $\mathbf{g}^s$, corresponds to the *slip condition*, during which relative motion occurs between the bodies (Fig. 3(a)).

Fig. 3(b) schematically represents the adopted cohesive law, i.e. the traction–separation model. The values $g^e_{n,max}$, and $g^e_{1,max}$, $g^e_{2,max}$ denote, respectively, the maximum normal and tangential displacements in the elastic phase, while $g^s_{n,max}$, $g^s_{1,max}$, and $g^s_{2,max}$ correspond to the displacements at complete interface separation. The values t_n^{max}, and τ_1^{max}, τ_2^{max} represent the maximum strength of the interface in the normal and tangential directions, respectively.

The interface response is initially linear elastic; therefore the stress vector $\mathbf{t}$ and the gap function $\mathbf{g}$ are linearly related according to

$$\mathbf{t} = \mathbf{K}\mathbf{g}^e = \mathbf{K}(\mathbf{g} - \mathbf{g}^s), \tag{6}$$

where $\mathbf{K}$ is the diagonal stiffness matrix, whose components K_{ii} determined from direct tensile and shear tests. Under the assumption of uncoupled elastic behavior, $\mathbf{K}$ is diagonal

$$\mathbf{K} = \begin{bmatrix} K_{nn} & 0 & 0 \\ 0 & K_{11} & 0 \\ 0 & 0 & K_{22} \end{bmatrix}, \quad \mathbf{g} = \begin{bmatrix} g_N \\ g_1 \\ g_2 \end{bmatrix}. \tag{7}$$

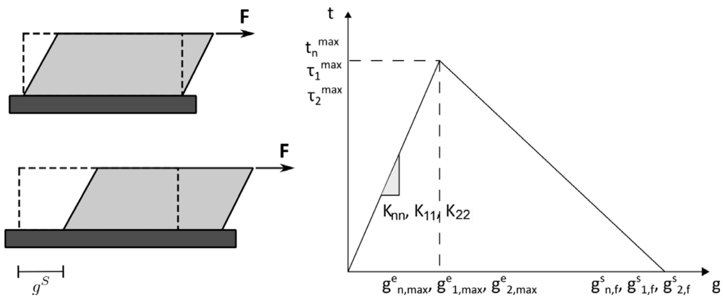

(a) (b)

Fig. 3. Stick condition (above) and slip condition (below) (a). Cohesive law: interface traction–separation model (b).

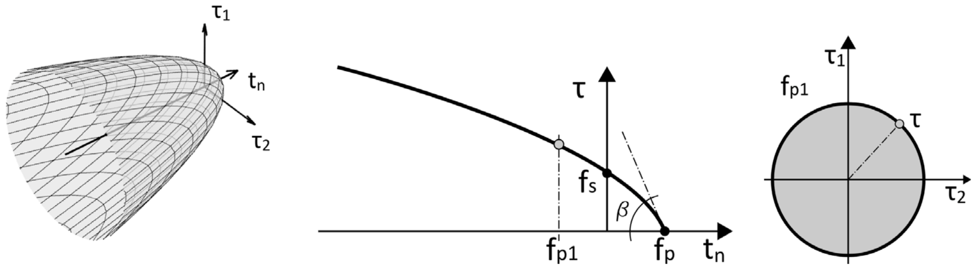

(a) (b) (c)

Fig. 4. Failure surface in 3D space (a). Failure surface in the plane of normal–tangential stress (b), and of shear stresses (c).

In practice, the normal elastic stiffness K_{11} and the tangential elastic stiffnesses K_{ii} (i=1,2) define the slope of the linear elastic portion of the cohesive response, with the assumption that $K_{11} = K_{22}$. In the present work, the stiffness matrix has been calibrated using classical peeling and shear delamination tests, and its coefficients are given by

$$K_{nn} = \frac{E}{t_0}, \quad K_{11} = K_{22} = \frac{\tau_2^{max}}{g^e_{2,max}}, \tag{8}$$

where E denotes the elastic modulus of the concrete and t_0 is the contact thickness.

The elastic domain of the cohesive zone is bounded by a quadratic failure surface $f(\mathbf{t}, f_p, f_s, \kappa, \beta) \leq 0$ (Fig. 4(a)), which explicitly captures the coupling between normal and tangential stress components. When represented in the $t_n - \tau$ stress plane, this surface provides a clear description of the normal–tangential interaction. It depends on the interface stress state, the normal and tangential interface strengths (f_p, f_s, respectively), an internal variable κ — commonly referred to as cumulative plastic slip — which governs the evolution of energy dissipation within the cohesive interface, and the apex angle β (Fig. 4(b) and Fig. 4(c)).

The failure function can be expressed as

$$f = \eta \left(\frac{\tau}{f_s}\right)^2 + \frac{q_s(\kappa)}{f_s}\left[\frac{\tau}{tg(\beta)} + t_n\right] - q_s(\kappa)\, q_p(\kappa)\, m \tag{9}$$

where m denotes the ratio between the normal and tangential strengths of the contact surface, defined as: $m = \frac{f_p}{f_s}$, and η is a parameter dependent on the hardening and softening functions in the normal (peeling) direction, $q_p(\kappa)$, and in the tangential (shearing) direction, $q_s(\kappa)$, through

$$\eta = \frac{q_p(\kappa)}{q_s(\kappa)} m - \frac{1}{tg(\beta)}. \tag{10}$$

The evolution of the interface strength is governed by the two scalar constitutive functions $q_p(\kappa)$ and $q_s(\kappa)$, which define the normal and tangential evolution of the failure surface, respectively, as functions of the equivalent inelastic displacement parameter κ, according to

$$t_n = q_p(\kappa) f_p, \quad \tau = q_s(\kappa) f_s. \tag{11}$$

The two functions are calibrated using experimental data from peeling and shearing tests.

The normal response is characterized by progressive softening: after reaching the peak tensile strength f_p, the normal cohesive strength decreases until a prescribed residual value is attained. Conversely, the tangential response exhibits an initial hardening

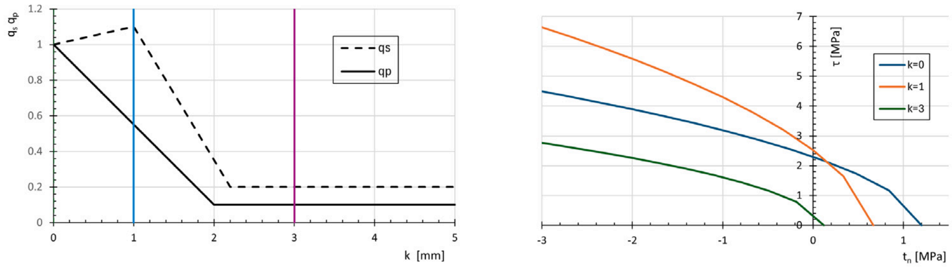

(a)   (b)

Fig. 5. Hardening/softening functions (a). Failure surface in the plane of normal–tangential stress (t_n - τ) for various values of κ (b).

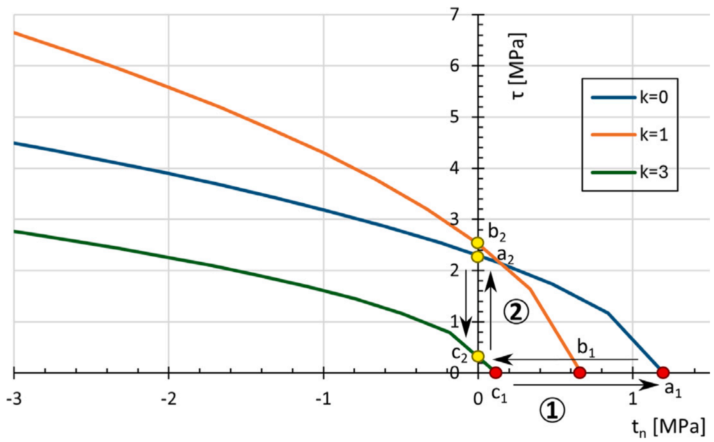

Fig. 6. Two representative stress paths: monotonic loading in pure normal tension (1) and pure tangential shear loading (2).

stage, in which the shear strength increases up to $1.1f_s$, in the example proposed in Fig. 5a, followed by progressive softening toward a residual tangential strength. This residual strength is introduced to phenomenologically represent the remaining shear-transfer capacity that may arise from mechanisms such as aggregate interlock or friction-like interactions after interface damage.

The combined evolution of q_p and q_s produces a continuous modification of the quadratic failure surface during loading, as illustrated in Fig. 5b. Three representative values of the internal variable are considered for visualization: $\kappa = 0$, corresponding to the undamaged interface; $\kappa = 1$, corresponding approximately to the maximum tangential strength; and $\kappa = 3$, representing the fully degraded state, where the interface reaches its prescribed residual strengths.

To illustrate the mechanical interpretation of the constitutive evolution, two representative stress paths are considered. The first corresponds to monotonic loading in pure normal tension (Fig. 6, load path 1), whereas the second represents pure tangential shear loading (Fig. 6, load path 2). These loading paths highlight the different roles of the constitutive functions q_p and q_s in governing the degradation of the interface under Mode I and Mode II dominated conditions.

Under monotonic normal tension (Path 1 in Fig. 6), the interface behaves elastically until the tensile strength f_p is reached. Thereafter, the normal cohesive traction decreases according to the softening law q_p until the prescribed residual tensile strength (taken as $0.1f_p$ in the present example) is attained (Fig. 7a).

Under pure shear loading (Path 2 in Fig. 6), the interface initially responds elastically up to the shear strength f_s. Subsequently, the tangential response undergoes a hardening phase, reaching a peak value of $1.1f_s$, followed by progressive softening toward the prescribed residual shear strength (taken as $0.2f_s$ in the present example), as shown in Fig. 7b.

Thus, this constitutive evolution enables the model to represent both the increase in shear resistance associated with inelastic interface mobilization and the residual load-carrying capacity to phenomenologically account for post-damage shear transfer, mainly (e.g., aggregate interlock and friction-like effects). The model itself does not explicitly simulate friction. In this regard, its validation under combined compression–shear loading would require dedicated experimental data.

To preserve a constant apex angle β throughout the evolution of the response, the following condition must be satisfied

$$q_s(\kappa) \leq q_p(\kappa)\ m\ tg(\beta). \tag{12}$$

The admissible range of β is constrained by: $tg^{-1}(1/m) \leq \beta \leq \pi/2$, as qualitatively shown in Fig. 8. Specifically, as β decreases, the surface progressively approaches a conical shape, whereas increasing β results in a paraboloidal surface.

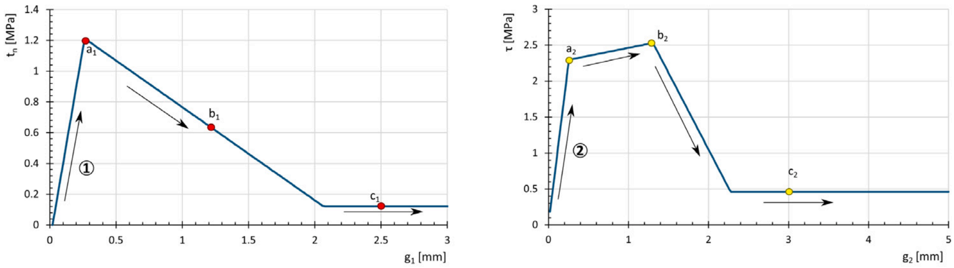

(a) (b)

Fig. 7. Softening in normal direction under monotonic loading in pure normal tension (a). Hardening under pure tangential shear loading (b).

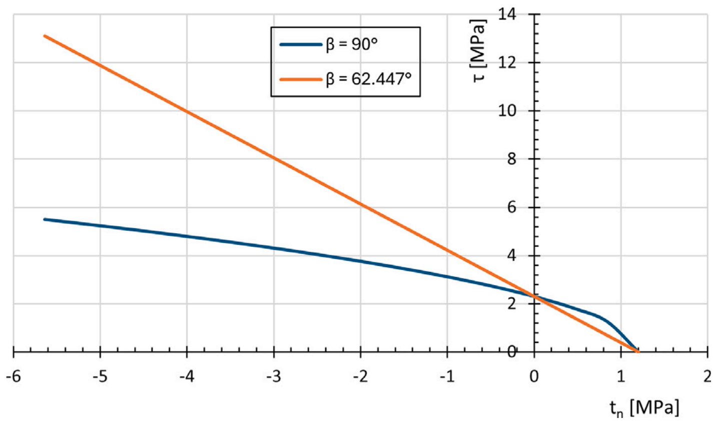

Fig. 8. Failure surface in the plane of normal–tangential stress (t_n - τ) for limit values of β.

The internal variable $\kappa = |tr(\mathbf{g}^s)|$ represents the cumulative inelastic displacement. When $q_p(\kappa) = q_s(\kappa) = 1$, the cohesive contact law reduces to a perfectly elasto-plastic formulation.

The evolution of the plastic displacement vector $\mathbf{g}^s$ is governed by a non-associated flow rule. Accordingly, the rate of the inelastic gap function $\dot{\mathbf{g}}^s$ and the plastic potential w are defined as follows

$$\dot{\mathbf{g}}^s = \gamma \frac{\partial w}{\partial \mathbf{t}}, \quad w = \eta \left(\frac{\tau}{f_s}\right)^2 + \frac{q_s(\kappa)}{f_s}\left[\frac{\tau}{tg(\beta)} + \langle t_n \rangle_+\right] - q_s(\kappa)\, q_p(\kappa)\, m, \tag{13}$$

where γ denotes the plastic multiplier.

From Eq. (13), it can be observed that under tensile normal stresses ($t_n > 0$), the Macaulay bracket is active ($\langle t_n \rangle_+ = t_n$) and the plastic potential coincides with the failure surface. Consequently, plastic evolution occurs simultaneously in the normal and tangential directions, enabling the coupled description of interface opening and sliding that characterizes mixed-mode fracture. Conversely, under compressive normal stresses ($t_n \leq 0$), the normal contribution to the plastic potential is suppressed by the Macaulay bracket ($\langle t_n \rangle_+ = 0$). As a consequence, the irreversible displacement evolves predominantly in the tangential direction while the compressive contact pressure remains governed by the contact constraints. Physically, this reflects the fact that compression tends to inhibit interface opening while simultaneously increasing the available shear resistance.

This leads to two distinct cases, illustrated in Fig. 9: (i) Tensile normal stress: the plastic potential coincides with the failure surface, resulting in an associated flow rule; (ii) Compressive normal stress: the plastic potential surface degenerates into a cylindrical shape, and the inelastic gap evolves exclusively in the tangential direction, i.e. $\frac{\partial w}{\partial t_n} = 0$.

Thus, the proposed plastic potential allows the interface response to naturally transition between tensile-dominated and compression-dominated loading conditions. This behavior is particularly relevant for interfaces in 3DPC, where compressive stresses generated by bending or transverse expansion may significantly modify the sliding resistance between adjacent layers.

2.4. Elasto-plastic problem formulation and numerical solution

The elasto-plastic response is computed using a classical return-mapping algorithm (Fig. 10(b)). First, an elastic predictor is evaluated to determine whether the current state remains within the elastic domain. If the consistency condition is satisfied, the increment is purely elastic. Otherwise, a plastic correction must be applied, computed as $\gamma \mathbf{K} \frac{\partial w}{\partial \mathbf{t}}$, by solving a nonlinear system that:

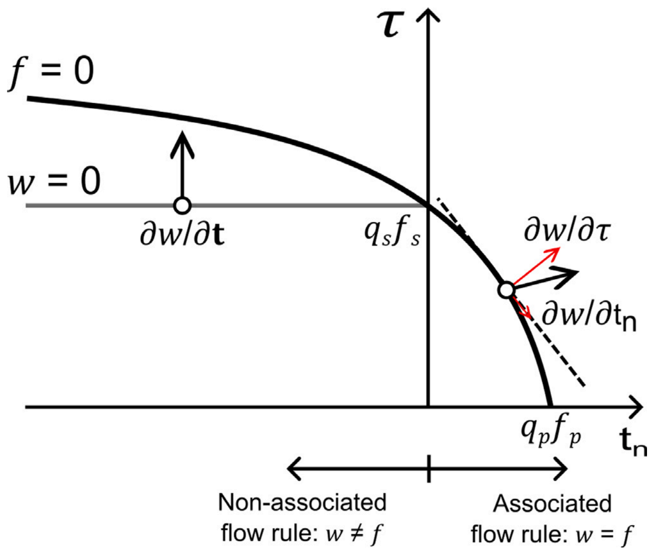

Fig. 9. Failure surface f and plastic potential w.

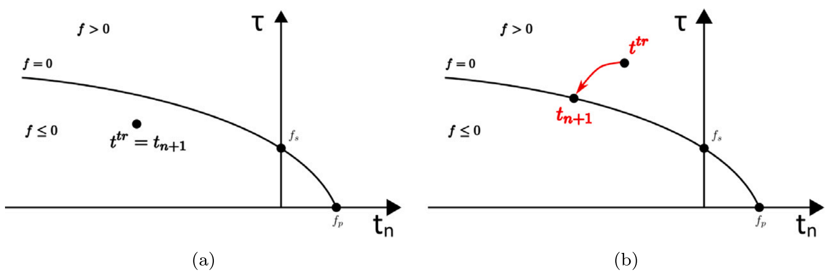

Fig. 10. Solution to the cohesive contact algorithm in the elastic (a) and plastic (b) domain.

(i) enforces the consistency condition $f(\mathbf{t},\kappa)$; (ii) minimizes the residual vector $\mathbf{r}$; and (iii) governs the evolution of the internal variable κ through the definition of an isotropic hardening variable h. These three conditions lead to the following system

$$\mathbf{b} = \begin{bmatrix} f(\mathbf{t}_{n+1},\kappa_{n+1}) \\ \mathbf{t}_{n+1} - \mathbf{t}^{tr}_{n+1} + \gamma\mathbf{K}\frac{\partial w}{\partial \mathbf{t}} \\ \kappa_{n+1} - \kappa_n - \dot{\kappa} \end{bmatrix} = \begin{bmatrix} f(\mathbf{t},\kappa) \\ \mathbf{r} \\ h \end{bmatrix} = \begin{bmatrix} 0 \\ 0 \\ 0 \end{bmatrix}, \tag{14}$$

where the unknowns are the stress $\mathbf{t}_{n+1}$ and the internal variable κ_{n+1} at the increment $n+1$, and the plastic multiplier γ. They are collected in a vector $\mathbf{x}$, with corresponding increment $\Delta\mathbf{x}$. The solution is obtained iteratively; at iteration k, the state variables are given by

$$\mathbf{x}^{kT} = \left[\mathbf{t}^k_{n+1},\ \kappa^k_{n+1},\ \gamma^k\right], \quad \Delta\mathbf{x}^T = [\Delta\mathbf{t},\ \Delta\kappa,\ \Delta\gamma]. \tag{15}$$

Applying a first-order Taylor expansion to the vector $\mathbf{b}$, and neglecting higher-order terms, yields

$$\mathbf{b}(\mathbf{x}^k + \Delta\mathbf{x}) = \mathbf{b}(\mathbf{x}^k) + \left.\frac{\partial \mathbf{b}}{\partial \mathbf{x}}\right|_{\mathbf{x}^k}\Delta\mathbf{x} + \cdots = 0. \tag{16}$$

The matrix of partial derivatives of the vector $\mathbf{b}$ is defined as

$$\mathbf{A} = \frac{\partial \mathbf{b}}{\partial \mathbf{x}} = \begin{bmatrix} \frac{\partial f}{\partial \mathbf{t}} & \frac{\partial f}{\partial \kappa} & \frac{\partial f}{\partial \gamma} \\ \frac{\partial \mathbf{r}}{\partial \mathbf{t}} & \frac{\partial \mathbf{r}}{\partial \kappa} & \frac{\partial \mathbf{r}}{\partial \gamma} \\ \frac{\partial h}{\partial \mathbf{t}} & \frac{\partial h}{\partial \kappa} & \frac{\partial h}{\partial \gamma} \end{bmatrix}. \tag{17}$$

At this stage, the increment of the unknown vector $\mathbf{x}$ can be computed as

$$\Delta\mathbf{x} = -(\mathbf{A}^k)^{-1}\mathbf{b}(\mathbf{x}^k) \tag{18}$$

Accordingly, at iteration $k+1$, the updated variables are given by

$$\mathbf{x}^{k+1} = \mathbf{x}^k + \Delta\mathbf{x}. \tag{19}$$

Further, the inelastic gap function is updated as

$$\dot{\mathbf{g}}^s = \gamma \frac{\partial w}{\partial \mathbf{t}}(\mathbf{t}_{n+1}^{k+1}, \kappa_{n+1}^{k+1})^T, \tag{20}$$

and

$$\mathbf{g}_{n+1}^s = \mathbf{g}_n^s + \dot{\mathbf{g}}^s. \tag{21}$$

A convergence tolerance is prescribed, and the iterative procedure is continued until $\|\mathbf{r}\| <$ toll and $|f| <$ toll.

Algorithm 1 PROCEDURE GETCONTACT

GETCONTACT(inc, ID, $\mathbf{g}_n$, $\Delta\mathbf{g}$, $\mathbf{g}_n^s$, κ_n, $\mathbf{t}_n$, $\mathbf{K}$, LOPENCLOSE)
LOPENCLOSE = 1 ▷ Closed contact
$\mathbf{g}_{n+1} = \mathbf{g}_n + \Delta\mathbf{g}$ ▷ Elastic trial
$\mathbf{g}_{n+1}^s = \mathbf{g}_n^s$
$\kappa_{n+1} = \kappa_n$
$q_p = q_p(\kappa_{n+1})$
$q_s = q_s(\kappa_{n+1})$
$\mathbf{t}_{n+1} = \mathbf{K}(\mathbf{g}_{n+1} - \mathbf{g}_n^s)$
$f^{tr} = f(\mathbf{t}_{n+1}, \kappa_n)$
if $f^{tr} > 0$ **then** ▷ Plastic corrector: return mapping
  $\mathbf{t}_{n+1}^{tr} = \mathbf{t}_{n+1}$
  res=1.0, $\gamma = 0,\ \mathbf{r} = 0,\ h = 0,\ \Delta\kappa = 0,\ \mathbf{x} = 0$
  while res > toll & $f >$ toll **do**
    $\mathbf{b} = [f\ \mathbf{r}\ h]$
    $\mathbf{A} = \begin{bmatrix} \frac{\partial f}{\partial \mathbf{t}} & \frac{\partial f}{\partial \kappa} & \frac{\partial f}{\partial \gamma} \\ \frac{\partial \mathbf{r}}{\partial \mathbf{t}} & \frac{\partial \mathbf{r}}{\partial \kappa} & \frac{\partial \mathbf{r}}{\partial \gamma} \\ \frac{\partial h}{\partial \mathbf{t}} & \frac{\partial h}{\partial \kappa} & \frac{\partial h}{\partial \gamma} \end{bmatrix}$
    $\Delta\mathbf{x} = \mathbf{A}^{-1}\mathbf{b}$
    $\mathbf{x} = \mathbf{x} + \Delta\mathbf{x}$
    $\mathbf{t}_{n+1} = \mathbf{x}[1:3],\ \kappa_{n+1} = \mathbf{x}[4],\ \gamma = \mathbf{x}[5]$
    res = $\|\Delta\mathbf{x}\|$
    $\dot{\mathbf{g}}^s = \gamma \frac{\partial w}{\partial \mathbf{t}}$ ▷ Variable update
    $\mathbf{g}_{n+1}^s = \mathbf{g}_n^s + \dot{\mathbf{g}}^s$
    $\Delta\kappa = tr(\dot{\mathbf{g}}^s)$
    $f = f(\mathbf{t}_{n+1}, k_{n+1})$
    $\mathbf{r} = \mathbf{t}_{n+1} - \mathbf{t}_{n+1}^{tr} + \mathbf{K}\dot{\mathbf{g}}^s$
    $h = \kappa_{n+1} - \kappa_n - \Delta\kappa$
    if $g_{n+1}^s(1) > g_{N,lim}^s$ **then** ▷ Contact opens
      LOPENCLOSE = 0
      $\mathbf{t}_{n+1} = 0$
      return
    end if
    $\mathbf{Q} = \mathbf{I} + \gamma\mathbf{K}\frac{\partial^2 w}{\partial \mathbf{t}^2} = \frac{\partial \mathbf{r}}{\partial \mathbf{t}}$
    $\mathbf{K} = \mathbf{Q}^{-1}\mathbf{K}$
  end while
end if
$\mathbf{g}_n^s = \mathbf{g}_{n+1}^s$
$\kappa_n = \kappa_{n+1}$.

The cohesive contact formulation was implemented in the FE software Abaqus [35] through the UINTER user subroutine, which collects the state variables of the two interacting surfaces and invokes the GETCONTACT procedure to evaluate interface stresses and inelastic displacements. The GETCONTACT procedure also governs contact opening: when the inelastic normal displacement g_{n+1}^s exceeds the limiting value $g_{N,lim}^s$, the tensile traction is set to zero and the contact is terminated.

Table 1
Constitutive parameters of the interfaces of the studied concretes (HP: High-performance; FR: Fiber-reinforced; NS: Natural sand).

	Type	K_{nn} [N/mm^3]	$K_{11} = K_{22}$ [N/mm^3]	f_p [MPa]	f_s [MPa]	β [°]	q_p –	q_s –
Mat. 1	HP	32 000	42	1.4	2.96	85	Fig. 11(a)	
Mat. 2	FR	21 600	42	1.25	2.96	85	Fig. 11(b)	
Mat. 3	NS	22 960	47	1.88	0.94	85	Fig. 11(c)	

3. Numerical results on various case studies

Three case studies are conducted, simulating experimental campaigns reported by different authors, covering various materials and testing methods. These data also allow for a comparison between two approaches to developing constitutive models for interfaces. The first two studies [8,11] are based directly on experimental measurements, whereas the latter studies [5,19] follow formulations provided in the CEB-FIP [39] and ACI [40] standards, which are typically used when experimental interface data are not available. The validity of the numerical implementation described in Section 2 is assessed by comparing the computed force–displacement responses with experimental results.

All numerical models are developed using Abaqus [35]. Experimental tests are reproduced by replicating specimen geometries, boundary conditions, and loading configurations. The modeling strategy for each case follows these steps:

- Definition of the elastic properties of 3DPC and the plastic response using the Concrete Damage Plasticity (CDP) model [41,42];
- Specification of the constitutive model for the interfaces, based either on direct tensile and shear tests (when available) or on established design standards;
- Construction of FE models with cohesive contact properties assigned to each interface;
- Comparison of numerical results with experimental data.

0 In addition to comparing numerical and experimental peak strengths and force–displacement responses, the stress state along the interfaces is examined to identify the onset and mode of failure, distinguishing between shear- and tension-dominated mechanisms.

The constitutive parameters of the interfaces of the studied concretes are summarized in Table 1.

The constitutive parameters adopted for the cohesive interfaces were determined according to the available experimental information for each material. The normal stiffness K_{nn} was calculated from the elastic modulus and the assumed interface thickness according to Eq. (8), whereas the tangential stiffnesses $K_{11} = K_{22}$ were calibrated from the initial elastic branch of the available shear tests whenever possible; otherwise, they were estimated consistently with the reported interface strength and displacement data. The normal interface strength f_p was directly obtained from tensile interface tests for Materials 1 and 2, while for Material 3 it was estimated from the concrete tensile strength using design-code-based relationships due to the absence of direct interface tensile measurements. Similarly, the tangential strength f_s was identified from experimental shear tests when available or, alternatively, estimated from established design-code or literature-based formulations.

Depending on the modeling strategy, the deposition (D-) and transition (T-) interfaces in 3DPC may be assigned identical or distinct mechanical properties. Specifically, D- and T- interfaces may exhibit different constitutive properties depending on the printing process, material composition, and curing conditions. In the present study, in the case of Material 3, where both interface types are involved, identical interface parameters were assigned to the D-interfaces and T-interfaces because the available experimental campaigns did not provide independent characterization of the two interface types. This choice avoids introducing additional unconstrained calibration parameters while allowing a consistent validation of the proposed constitutive framework.

The hardening/softening functions q_p and q_s were calibrated using post-peak experimental responses whenever these data were available; otherwise, physically consistent degradation laws were assumed and explicitly identified as modeling assumptions. Finally, the apex angle β was set equal to 85° for all simulations, providing a nearly parabolic failure envelope while ensuring numerical stability and satisfying the admissibility condition of the proposed constitutive formulation.

It is specified that the constitutive parameters adopted in the present study should be interpreted as calibrated model parameters rather than uniquely identified material properties. Their calibration follows the amount of experimental information available for each material. Consequently, different parameter sets may produce similar global structural responses, particularly when only macroscopic force–displacement curves are available. The objective of the present work is therefore not to establish a unique inverse identification procedure, but rather to demonstrate that physically motivated interface parameters calibrated from available experimental data provide consistent predictions across different loading configurations.

3.1. Calibration of concrete parameters for the CDP model

The compressive response of concrete is reproduced using the uniaxial formulation proposed in [43]

$$\sigma_c = \frac{E_0 \varepsilon_c}{1 + \left[\frac{E_0 \varepsilon_p}{\sigma_p} - 2\right]\left(\frac{\varepsilon_c}{\varepsilon_p}\right) + \left(\frac{\varepsilon_c}{\varepsilon_p}\right)^2}, \tag{22}$$

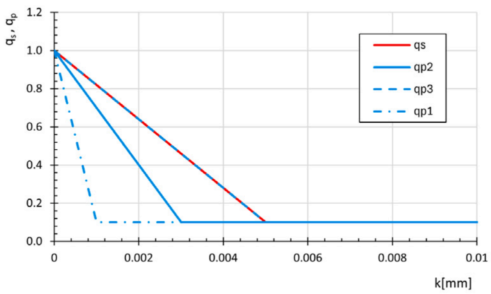

(a) Mat 1.

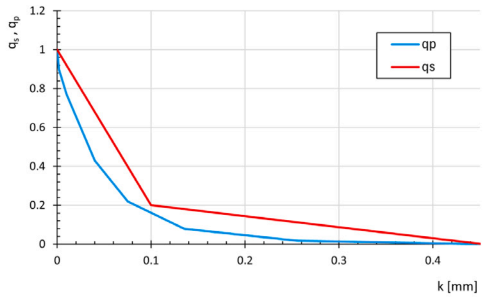

(b) Mat 2.

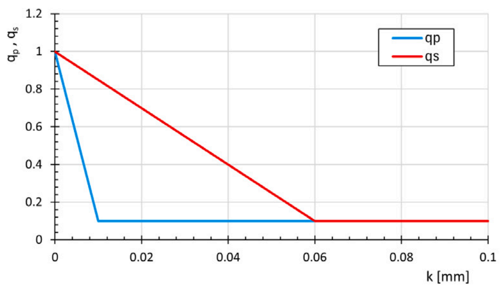

(c) Mat 3.

Fig. 11. Computed hardening/softening functions of the studied concretes (see the corresponding case studies for detailed discussion).

where E_0 is the undamaged elastic modulus, σ_c and ε_c are the stress and strain in the concrete, while σ_p and ε_p denote the maximum stress and strain within the elastic regime.

The tensile strength f_{tu} is calculated using the equation provided by the CEB-FIP Model Code [39], as a function of the characteristic compressive strength f_{cu}

$$f_{tu} = 0.3\,(f_{cu})^{2/3}. \tag{23}$$

In the absence of experimental data, the post-peak softening branch of the tensile stress–crack opening curve is reconstructed following the formulation proposed by [44]

$$\frac{\sigma_t}{f_{tu}} = \left[1 - \left(c_1 \frac{w_t}{w_{cr}}\right)^3\right] e^{-c_2 \frac{w_t}{w_{cr}}} - \frac{w_t}{w_{cr}}(1 - c_1^3) \quad e^{-c_2}, \tag{24}$$

where σ_t is the tensile stress in the concrete, c_1 and c_2 are constants equal to 3.0 and 6.93 respectively, w_t is the crack width, and w_{cr} is the critical crack opening displacement (in mm) at which complete cracking occurs, calculated as

$$w_{cr} = 5.14\,\frac{G_F}{f_{tu}}, \tag{25}$$

with G_F fracture energy, determined using the CEB-FIP relationship [39]

$$G_F = 0.73 f_{cm}^{0.18}, \tag{26}$$

with

$$f_{cm} = f_{cu} + 8 \text{ MPa}. \tag{27}$$

Once the uniaxial compressive and tensile behavior is determined, the corresponding damage coefficients are calculated as

$$d_c = 1 - \frac{\sigma_c}{f_{cu}}, \quad d_t = 1 - \frac{\sigma_t}{f_{tu}}, \tag{28}$$

where d_c and d_t denote the damage variables under compressive and tensile loading, respectively.

The inelastic strain curves are then derived by computing the elastic strain $\varepsilon_{el} = \sigma/E_0$ and obtaining the inelastic component as the difference

$$\varepsilon_{in} = \varepsilon - \varepsilon_{el}. \tag{29}$$

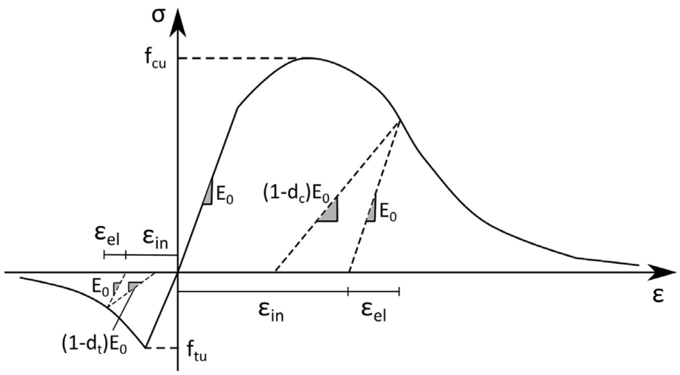

Fig. 12. Inelastic strain curves for the Concrete Damage Plasticity (CDP) model.

Table 2
Elastic properties of the studied concretes (HP: High-performance; FR: Fiber-reinforced; NS: Natural sand).

	Type	Direction	E_0 [MPa]	ρ [ton/mm^3]	f_{cu} [MPa]	f_{tu} [MPa]	ν –
Mat 1	HP	–	32 000	2.4E−09	78.0	–	0.2
Mat 2	FR	D1	21 900	2.2E−09	45.1	2.45	0.2
		D3	21 600	2.2E−09	38.2	1.25	0.2
Mat 3	NS	–	22 960	2.5E−09	21.8	2.56	0.2

Fig. 12 provides a schematic representation of the CDP model.

The elastic properties of the studied concretes are reported in Table 2, where ρ is the specific weight, and ν the Poisson's ratio.

For completeness, the remaining parameters required to fully define the material for CDP implementation are: the dilation angle $\alpha = 36°$ [45]; the parameter $K_c = 2/3$ [46]; the biaxial-to-uniaxial compressive strength ratio $f_{b0}/f_{c0} = 1.16$ [46]; the eccentricity $e = 0.1$ [5]; and the viscosity parameter $\zeta = 0.0005$ [5].

It should be emphasized that the role of the CDP model in the present work is to describe the constitutive response of the bulk concrete matrix, whereas the anisotropic mechanical behavior of the printed material is introduced primarily through the explicit modeling of the interlayer interfaces by means of the proposed cohesive contact formulation. This modeling strategy enables the numerical framework to distinguish between matrix-dominated and interface-dominated failure mechanisms, depending on the loading direction and the orientation of the printed layers. For example, in the direct tensile test of Material 2 along the D1 direction, where the interfaces are parallel to the applied load, failure is governed predominantly by tensile damage within the concrete matrix and is therefore controlled by the CDP model. Conversely, in the D3 direction, where the interfaces are loaded in tension, failure is governed by interlayer decohesion and is controlled primarily by the cohesive contact formulation.

The adoption of an isotropic CDP model implies that possible anisotropic effects within the printed filaments themselves are neglected. Consequently, the proposed formulation may underestimate or overestimate the contribution of printing-induced anisotropy associated with the bulk material. Nevertheless, this assumption is considered appropriate for the present validation cases, since the dominant source of anisotropy arises from the interlayer interfaces, whose behavior is explicitly modeled through the cohesive contact algorithm. For materials exhibiting pronounced intra-filament anisotropy, however, a direction-dependent constitutive model, such as an orthotropic damage or plasticity formulation, would provide a more realistic representation of the bulk material response and could be naturally combined with the proposed interface formulation.

3.2. Case study 1: high-performance concrete

The direct tensile and Iosipescu shear tests presented in [8], used to characterize 3DPC interfaces, are adopted in this study. The material considered is a purpose-designed high-performance concrete, whose elastic properties correspond to *Material 1* in Table 2.

The experimental results from the tensile test indicate a brittle response of the material, reaching peak stress linearly and then failing completely, without any development of strength in the plastic phase. Consequently, among the interface constitutive parameters, only those associated with the elastic phase can be uniquely identified. These parameters are summarized in Table 1 and referred to as *Material 1*.

In the normal direction, three hardening/softening functions are defined to investigate the influence of plastic evolution on the mechanical response (see Fig. 11(a)). The values of the inelastic accumulation variable κ are set to 0.001 mm for q_{p1}, 0.003 mm for q_{p2}, and 0.005 mm for q_{p3}. As κ increases, the fracture energy — represented by the area under the hardening/softening curve — increases accordingly, resulting in a more pronounced softening phase.

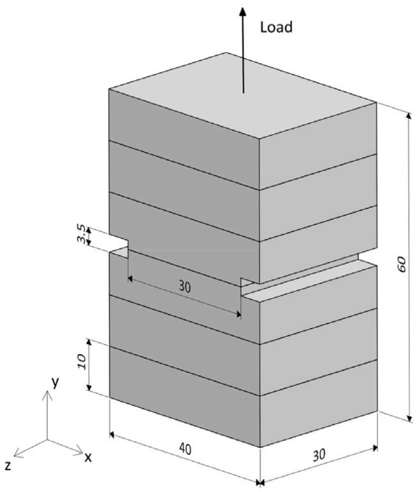

Fig. 13. Schematic representation of the direct tensile test.

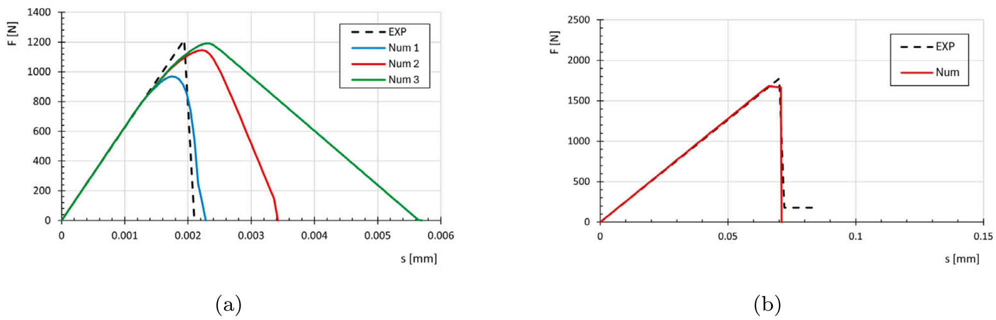

Fig. 14. Material 1: force–displacement results for the direct tensile test (a) and the Iosipescu shear test (b).

In the tangential direction, it is not possible to directly reconstruct the function q_s from the available experimental data. Therefore, a linear degradation of the shear strength is assumed, decreasing to zero at $\kappa = 0.005$ mm, consistent with the value adopted for q_{p3}, as shown in the same figure.

All test specimens were mechanically extracted from a single 3D-printed wall in order to ensure consistency of the key printing and material parameters, including climatic conditions, layer height, nozzle speed, nozzle stand-off distance, and the time interval between successive layer depositions.

3.2.1. Direct tensile test

The direct tensile test is performed on the notched prism shown in Fig. 13, with a tensile load applied in the y-direction at a displacement rate of 0.25 mm/min. The imposed displacement and the corresponding force were recorded throughout the test.

In the numerical model of the direct tensile test, the lower surface is fully constrained, that is: $\mathrm{U}_x = \mathrm{U}_y = \mathrm{U}_z = 0$. All nodes on the upper surface are coupled to a reference point via a coupling constraint, to which a vertical displacement of 0.06 mm is applied.

The force–displacement curves reported in Fig. 14(a) show the total reaction force and the displacement of the reference point along the loading direction for the three hardening/softening functions considered. The influence of the different assumptions adopted for the plastic evolution in the contact law is clearly evident, as increasing the fracture energy leads to higher peak loads. Specifically, for an experimental peak load of 1214 N occurring at a displacement of 0.00194 mm, the third hardening/softening law provides the closest agreement with the experimental response, yielding a peak load of 1192 N at a displacement of 0.0022 mm. By comparison, the first and second softening laws result in peak loads of 978 N and 1146 N, respectively.

The stress distribution in the loading direction at peak load is shown in Fig. 15(a). The stresses reach the maximum interface normal strength of 1.4 MPa before the onset of plasticity, as obtained by dividing the experimental peak force of 1214 N by the interface area (A = 900 mm^2). The same stress level is attained at the central interface, whereas all other interfaces exhibit lower peak stress values (Fig. 15(b)).

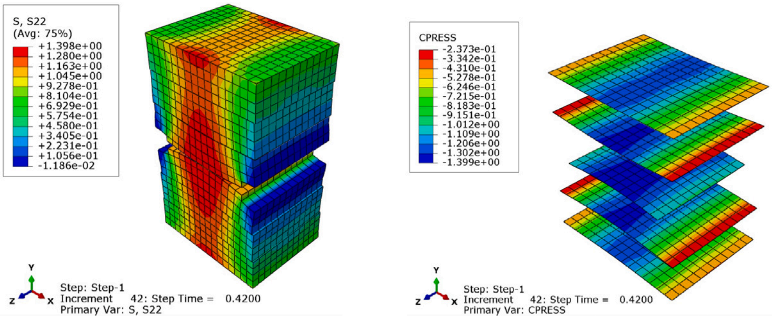

(a) (b)

Fig. 15. Material 1: maximum stress distribution in the loading direction in the direct tensile test (a); maximum interface pressure distribution in the direct tensile test (b).

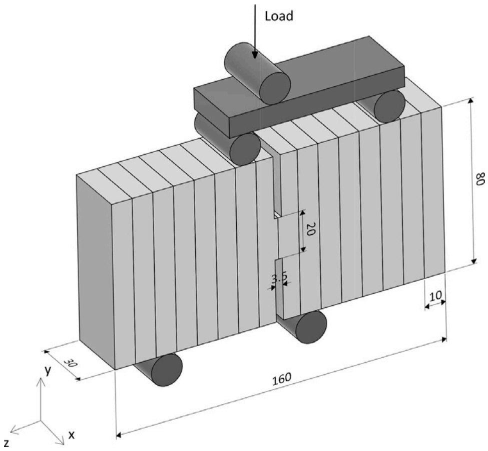

Fig. 16. Schematic representation of the Iosipescu shear test configuration.

3.2.2. *Iosipescu shear test*

The Iosipescu shear test is performed on the notched prism shown in Fig. 16. The load is applied as a displacement-controlled input at a rate of 0.25 mm/min in the y-direction and is transmitted through two connected cylindrical rollers that are free to rotate. The primary objective of this test is to induce a nearly pure shear stress state at the central interface, with negligible bending moment, leading to a Mode II failure of the specimen.

In the numerical model of the Iosipescu shear test, two lower supports are introduced, where the displacements $U_x = U_y = U_z$ are fully constrained. A reference point, aligned with the central interface, is subjected to a prescribed displacement of 0.1 mm. The reference point is connected to two 10 mm-wide loading surfaces corresponding to the roller positions through a coupling constraint.

Based on the results obtained from the direct tensile test, the hardening/softening function q_p associated with q_{p3} (Fig. 11(a)) is adopted for the interface response.

The force–displacement response is reported in Fig. 14(b), where the reaction force in the loading direction at the reference point is plotted against the tangential displacement of a node located on the central interface. A satisfactory agreement with the experimental results is observed in the elastic regime, up to a peak load of 1682 N at a displacement of 0.066 mm, compared to the experimental values of 1775 N and 0.07 mm.

In the numerical simulation, once the elastic limit is reached, complete failure occurs with full separation of the specimen into two parts. Consequently, as in the experimental test, the post-peak (plastic) branch of the force–displacement curve cannot be captured numerically, although the maximum shear strength is accurately reproduced.

The contour plot in Fig. 17(a) shows the von Mises stress distribution at the peak load, revealing a diagonal failure pattern across the central interface, which is characteristic of this testing configuration. Following failure, the specimen separates into two distinct parts, as shown in Fig. 17(b).

An analysis of the tangential stresses developing along the interfaces indicates that failure is localized at the central interface, while the remaining interfaces do not reach the maximum shear strength (Fig. 18(a)). This behavior is consistent with the experimentally observed failure mode shown in Fig. 18(b).

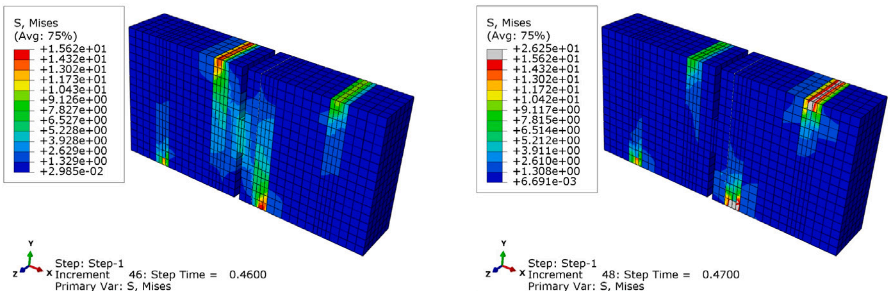

(a) (b)

Fig. 17. Material 1: von Mises stress distribution at peak load (a) and at failure (b).

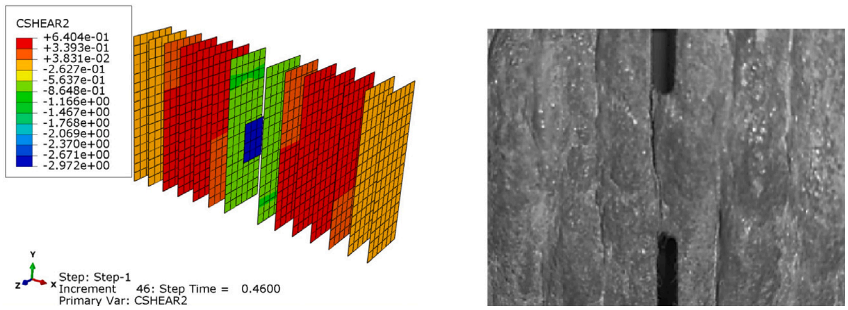

(a) (b)

Fig. 18. Material 1: maximum shear stress distribution along the interfaces (a) and experimental specimen failure observed in [8] (b).

3.3. Case study 2: fiber-reinforced concrete

The second material considered is taken from the study by [11]. The experimental campaign includes direct tensile tests in the D1, D2, and D3 directions, as well as four-point bending tests. The material is a fiber-reinforced concrete, whose elastic properties correspond to *Material 2* in Table 2. Depending on the printing direction of the deposited filaments, the elastic properties differ depending on whether the loading direction is longitudinal (D1) or orthogonal to the laying plane (D3).

For interface characterization, only the D2 and D3 directions are relevant. Specifically, the transverse direction (D2) is not considered in the present study because the force–displacement curves required to reconstruct a traction–separation law are not reported. Further, the tests were performed on specimens composed of single filaments, which do not form an interface between adjacent layers. The constitutive parameters adopted for the interface are summarized in Table 1 and are referred to as *Material 2*.

For Material 1, the hardening/softening functions were assumed due to the absence of complete post-peak experimental data. For Material 2, the post-peak response in the normal direction is available and exhibits an exponential decay, which enables the definition of the q_p function. In the tangential direction, the q_s function is again assumed and is defined to follow the same trend as q_p, as shown in Fig. 11(b).

As in the previous case study, all specimens are extracted from a single 3D-printed element to ensure consistent printing parameters throughout the experimental campaign.

3.3.1. Direct tensile test

Direct tensile tests were conducted along the principal directions D1 and D3, with the results reported as force–CMOD curves, where CMOD (Crack Mouth Opening Displacement) is the crack opening measured at the failure zone using clip gauges.

For the longitudinal (D1) and perpendicular (D3) directions, the same notched prism geometry shown in Fig. 13 is adopted. A schematic representation of the test configuration in the D1 direction is shown in Fig. 19.

The numerical models are subjected to the same boundary and loading conditions adopted for Material 1 (Section 3.2), with the lower surface fully constrained ($U_x = U_y = U_z = 0$) and the upper surface connected to a reference point, to which a vertical displacement of 2 mm is applied in the D1 direction and 0.45 mm in the D3 direction.

Direction D1

Failure in the D1 direction is governed by the tensile strength of the bulk concrete, as the interfaces are oriented parallel to the loading direction, and the presence of interfaces has a negligible influence on the ultimate capacity. The results obtained for

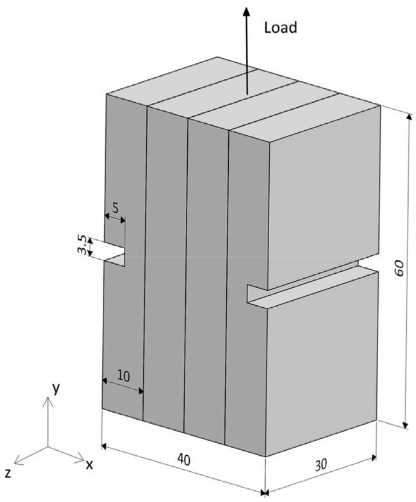

Fig. 19. Schematic representation of the direct tensile test in direction D1.

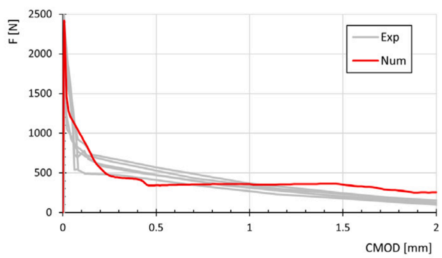

(a)

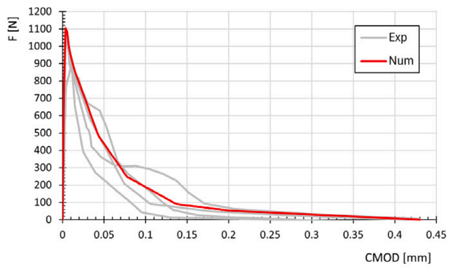

(b)

Fig. 20. Material 2: results of the direct tensile tests in the D1 (a) and D3 (b) direction.

the D1 direction are shown in Fig. 20(a), where the total reaction force in the loading direction at the reference point is plotted against the corresponding displacement. Good agreement with the experimental data is achieved, with a numerical peak load of 2414 N at a displacement of 0.0073 mm. The experimental test reports a maximum force of 2113 N at a displacement of 0.0064 mm, corresponding to a difference of approximately 14%. This result confirms that the CDP model accurately reproduces the material response in the D1 direction.

An analysis of the normal and tangential stresses at the interfaces at peak load indicates that both remain within the elastic regime, with tensile failure occurring entirely within the concrete matrix (Fig. 21(b) and Fig. 21(c)). The stresses in the loading direction increase up to a maximum value of 2.88 MPa (Fig. 21(a)), compared to 2.45 MPa measured experimentally, marking the onset of tensile damage that propagates through the central zone until complete failure.

Direction D3

The D3 direction characterizes a loading perpendicular to the interfaces, which activates interlayer decohesion and limits the attainable tensile strength to that of the interfaces. Thus, in this case failure is governed by the tensile capacity of the interfaces, leading to premature cracking.

The results obtained for the D3 direction are shown in Fig. 20(a) as force–CMOD curves. In this case, a clear softening branch develops after the peak strength, extending from a CMOD of 0.0032 mm up to 0.43 mm, which allows for a complete definition of the interface constitutive model.

The juxtaposition of numerical and experimental results demonstrates strong agreement with the experimental observations. The maximum force obtained numerically is 1106 N, compared to 1007 N in the experiment, corresponding to a difference of 9.83%. The displacements are 0.0034 mm and 0.0032 mm, respectively, representing a variation of 6.25%.

At peak load, the stress distribution along the loading direction is shown in Fig. 22(a), with the maximum normal stress at the central interface reaching 1.25 MPa (Fig. 22(b)). Subsequently, the softening branch develops until complete specimen separation.

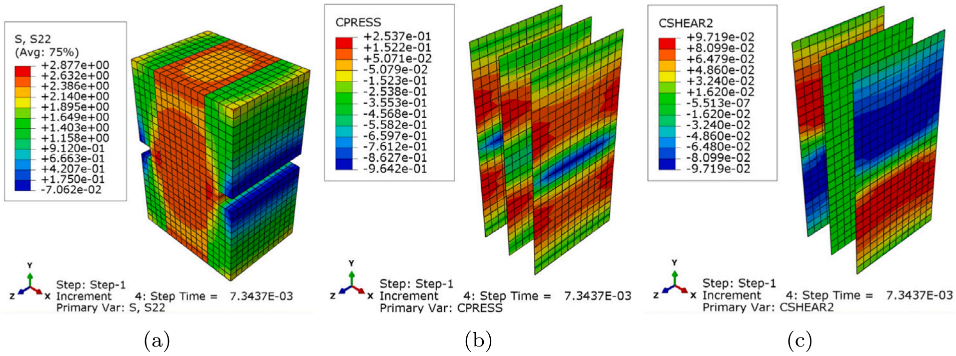

Fig. 21. Material 2: contour plots of the direct tensile test in direction D1: maximum tensile stresses (a); maximum interface pressure distribution (b); maximum shear stress distribution along the interfaces (c).

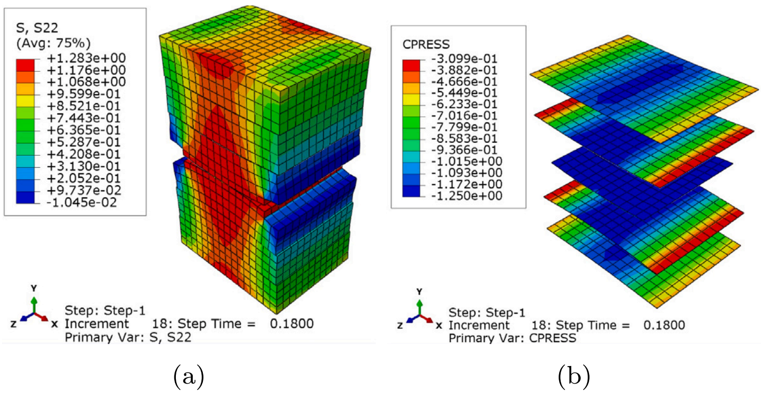

Fig. 22. Material 2: contour plots of the direct tensile test in direction D3: maximum stress distribution in the loading direction (a); maximum interface pressure distribution (b).

3.3.2. Four-point bending test

Four-point bending tests were conducted on the specimens, as illustrated in Fig. 23, with the load applied in the y-direction via two loading cylinders spaced 50 mm apart. The same loading protocol used for the direct tensile tests was applied: a displacement rate of 0.2 mm/min during the elastic phase, 0.01 mm/min to capture the peak strength, and 0.1 mm/min to characterize the post-peak softening behavior.

All results are presented as force–CMOD curves. The investigated directions include the longitudinal direction D1 (Fig. 23(a)) and the perpendicular direction D3 (Fig. 23(b)).

In the numerical models, the boundary conditions consist of two linear supports: one fully restraining all translational degrees of freedom, and the other allowing horizontal translation. Loads are applied at the same positions as in the experimental setup, with imposed displacements of 3 mm for direction D1 and 1 mm for D3. To obtain the numerical force–CMOD curves, the reaction forces in the loading direction at the loading points and the horizontal displacement of a control node at the notch are extracted from the simulations.

Direction D1

The numerical model for direction D1 produced the force–CMOD curve shown in Fig. 24(a). Agreement with the experimental peak load of 982 N is observed, with a numerical value of 913 N, corresponding to a 7% deviation. This result confirms that the flexural strength in the longitudinal direction is primarily governed by the tensile strength of the printed concrete, while the contribution of the interfaces is minimal.

Analysis of the stresses in the z-direction and the evolution of tensile damage shows that, once the peak tensile strength of 2.5 MPa (approximately f_{tu} of Material 2) is reached (Fig. 25(a)), tensile damage initiates (Fig. 25(c)) and progressively evolves until complete failure of the specimen (Fig. 25(d)). Although the interfaces are subjected to shear forces due to layer sliding, the maximum tangential stress never exceeds the shear strength at peak load (Fig. 25(b)), confirming that their effect in this loading direction is negligible.

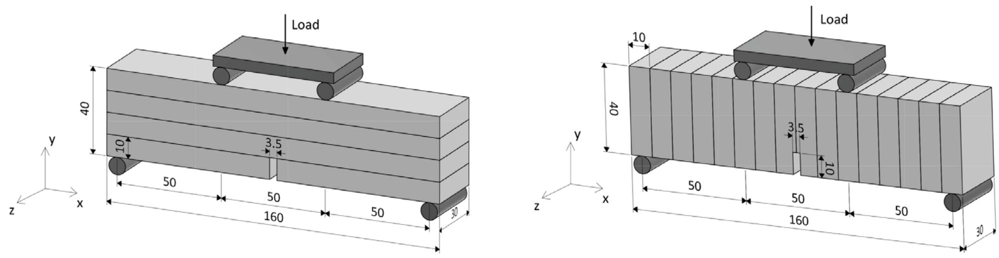

(a) (b)

Fig. 23. Schematic representation of the four-point bending test in the longitudinal direction D1 (a) and perpendicular direction D3 (b).

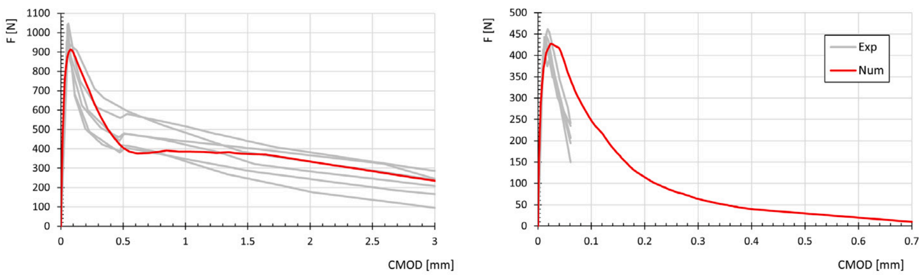

(a) (b)

Fig. 24. Material 2: results of the four-point bending tests in the D1 (a) and D3 (b) direction.

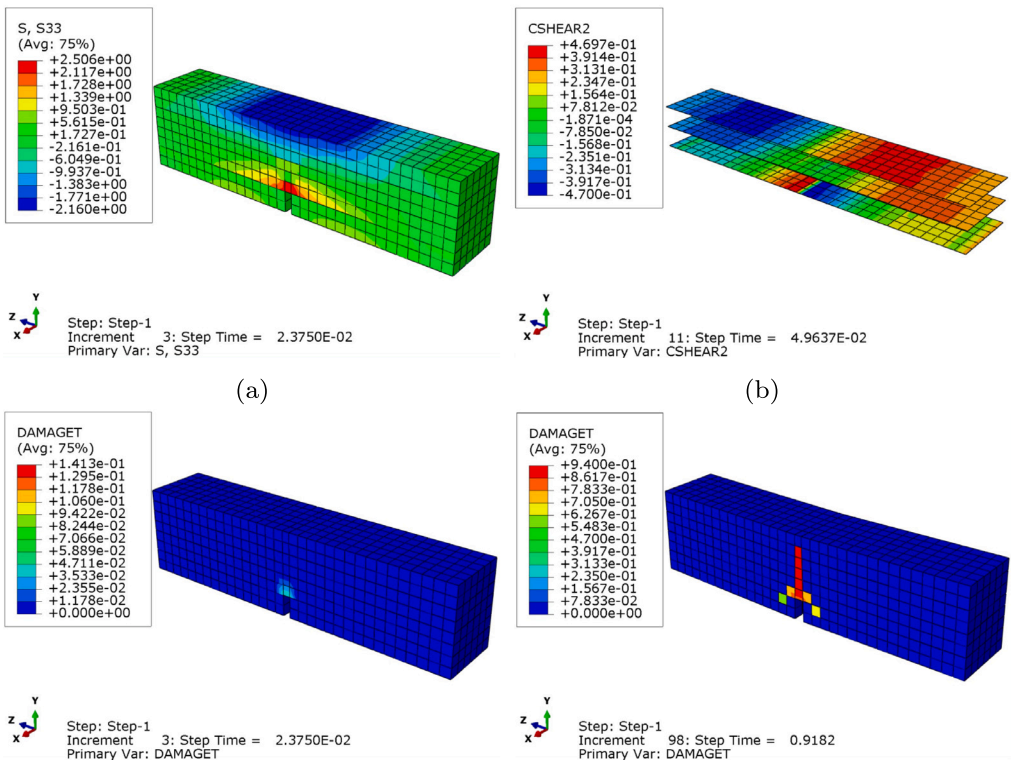

(c) (d)

Fig. 25. Material 2: contour plots for the four-point bending test in direction D1: tensile stresses at the onset of damage (a); maximum shear stresses distribution along the interfaces (b); initiation of tensile damage (c); specimen failure (d).

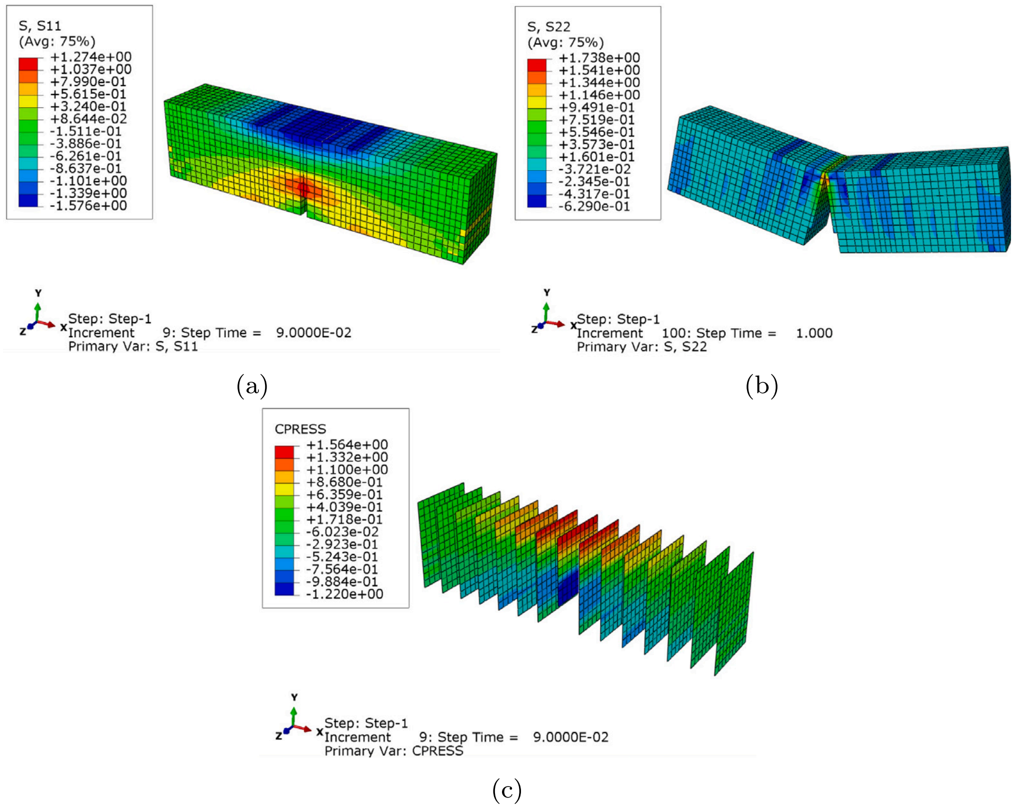

Fig. 26. Material 2: contour plots for the four-point bending test in direction D3: maximum tensile stresses (a); specimen failure (b); maximum interface pressure distribution (c).

Direction D3

In direction D3, failure is governed by the normal cohesive strength of the contact surfaces, as bending induces tensile stresses orthogonal to the interfaces.

Fig. 24(b) compares the experimental and numerical force–CMOD curves. The peak forces obtained are 444 N and 427 N, respectively, corresponding to a difference of 3.83%. The numerical model also captures the post-peak behavior, which exhibits an exponential softening trend, consistent with the modeling assumptions and the tensile test results along direction D3.

Specimen failure localizes along the central interface once the ultimate tensile stress is reached (Fig. 26(c)), followed by decohesion leading to complete fracture (Fig. 26(a) and Fig. 26(b)). It is noteworthy that the maximum stress in D3 is approximately 50% lower than in D1, and the failure is brittle: once cracking initiates, it rapidly propagates along the interface separation line.

Finally, as an illustrative exercise, the force–CMOD curve obtained for Material 2 is compared with that predicted using the interface properties of Material 1 (Section 3.2). As shown in Fig. 27, differences in the hardening/softening functions influence not only the post-peak behavior but also the flexural strength in D3 direction. Specifically, using the interface parameters from Material 1 yields a peak load of 371 N, which is 13.11% lower than that obtained for Material 2.

3.4. *Case study 3: natural sand concrete*

In the third case study, the experimental tests reported by [19] are reproduced numerically. The elastic properties of the 3DPC, listed in Table 2 as *Material 3*, are consistent with those of an ordinary concrete made with natural sand. Compression tests and four-point bending tests were performed on 3D-printed specimens under loading applied along three orthogonal directions, and the results are compared with those obtained from homogeneous (cast) specimens. All 3D-printed specimens were mechanically extracted from a previously manufactured plate.

Given the limited availability of force–displacement data from direct tensile and shear tests on 3D-printed elements, the third case study characterizes the material interfaces following the approach proposed by [5], based on design standards such as CEB-FIP Model Code [39]. In this approach, the interface tensile strength f_p is assumed equal to the concrete tensile strength f_{tu}, while the concrete compressive strength f_{cu} is taken as the average value of the experimentally measured compressive strengths along the three principal loading directions, equal to 21.8 MPa.

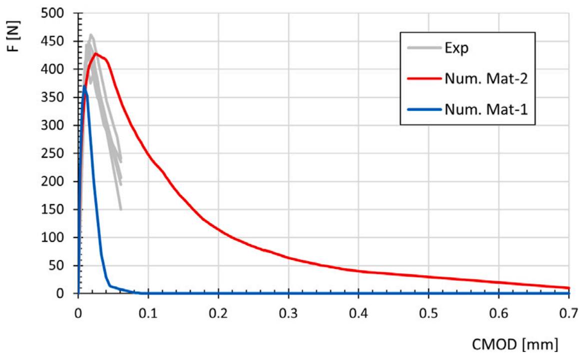

Fig. 27. Comparison of numerical results for the four-point bending test in the D3 direction using the interface properties of Materials 1 and 2.

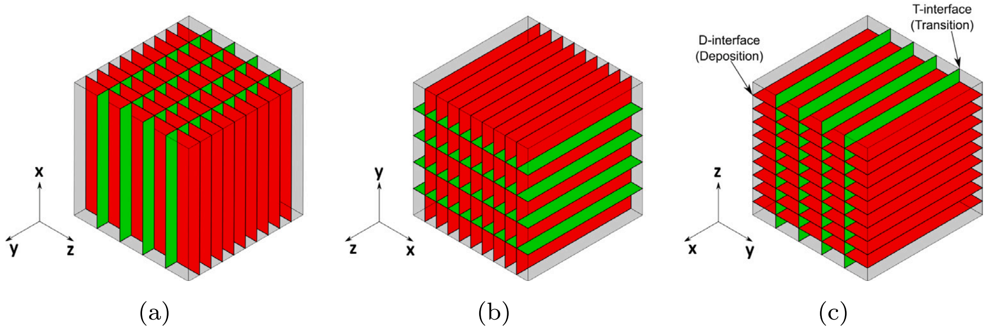

Fig. 28. Compression test loading directions: X (a), Y (b), and Z (c).

The shear strength of the interfaces is calculated following the CEB–FIP Model Code [39] as: $f_s = \tau_a + \mu\ \sigma_c$, where τ_a represents the adhesive bonding and mechanical interlocking stress between the two contact surfaces, μ is the friction coefficient, and σ_c is the confining pressure. The value for f_s reported in the literature is adopted and set equal to 0.94 MPa.

The tangential softening function q_s is defined according to a triangular traction–separation cohesive law, as illustrated in Fig. 3(b), with a peak displacement $g^e_{1,max} = g^e_{2,max} = 0.02$ mm followed by a linear softening up to $g^s_{1,max} = g^s_{2,max} = 0.08$ mm. This corresponds to a tangential elastic stiffness of $K_{11} = K_{22} = 47$ N/mm^3.

In the normal direction, the elastic stiffness K_{nn} is set equal to the elastic modulus of the concrete E_0. No post-peak inelastic phase is defined for the normal direction; the normal softening function q_p is assumed based on a study by [6], with a maximum separation $g^s_{n,max} = 0.01$ mm.

The complete set of cohesive law parameters is summarized in Table 1 as *Material 3*, and the corresponding hardening/softening functions are plotted in Fig. 11(c). Unlike the classical triangular traction–separation law, where the stress drops to zero at the ultimate displacement, the present model assumes residual normal and tangential strengths equal to $0.1 f_p$ and $0.1 f_s$, respectively, leveraging the extended capabilities of the implemented code.

3.4.1. Compression test

The specimens used for compression testing are cubic, with a side length of 100 mm, and are composed of filaments 20 mm wide and 10 mm high. The specimens are loaded along the three principal directions defined in Fig. 28.

In the analyzed specimens, both deposition interfaces (D-interfaces) and transition interfaces (T-interfaces) are present, with orientations that depend on the loading direction. In the absence of experimental evidence distinguishing the mechanical behavior of the two interface types, they are assumed to share identical contact properties.

The boundary conditions are identical for all three models and are applied to different surfaces according to the considered loading direction. A vertical displacement of 1 mm is imposed on the top surface, while translational degrees of freedom in the plane orthogonal to the loading direction are restrained. The bottom surface is fully fixed, with $\mathrm{U}_x = \mathrm{U}_y = \mathrm{U}_z = 0$.

Fig. 29(a) shows the stress–displacement curves obtained from the numerical simulations of the three compression tests on the 3DPC samples, alongside the results from the cast specimen. The peak stresses are extracted from these curves and compared with the experimental measurements (Fig. 29(b)). The comparison demonstrates that the anisotropic behavior of the material is accurately captured, with $\mathrm{F}_y > \mathrm{F}_z > \mathrm{F}_x$, particularly for F_x and F_z. The largest deviation is observed in the F_y direction.

Fig. 30 shows the interface shear stress (Fig. 30(a), Fig. 30(d) and Fig. 30(g)) and normal pressure (Fig. 30(b), Fig. 30(e) and Fig. 30(h)) at peak compressive load, along with the tensile damage (Fig. 30(c), Fig. 30(f) and Fig. 30(i)) in the concrete at the end of the analysis.

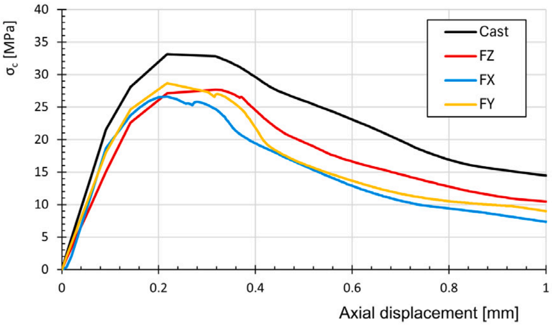

(a)

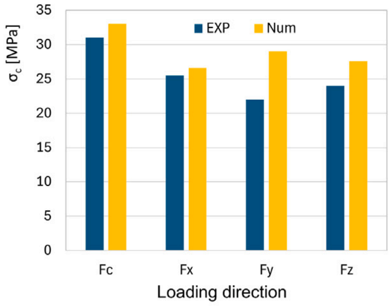

(b)

Fig. 29. Material 3: results of the compression tests (a) and comparison with experimental peak stresses (b).

In all loading directions, failure is governed by interfacial shear, while the concrete tensile strength is never exceeded. Shear failure occurs on both D- and T-interfaces in the X direction, is concentrated on T-interfaces in the Y direction, and on D-interfaces in the Z direction. Consequently, when separation surfaces are oriented orthogonally to the loading direction, failure is triggered by interfacial sliding due to the Poisson effect (transverse expansion). This likely explains the discrepancy observed in the Y direction, where the global compressive response depends on the transition interfaces, which were assumed to share the same properties as the deposition interfaces, though they may differ in reality.

3.4.2. Four-point bending test

The flexural strength of the material is evaluated through four-point bending tests performed on prismatic specimens with dimensions of 90 × 90 × 360 mm. Both homogeneous (cast) and 3D-printed specimens are considered; the latter consist of filaments 30 mm wide and 15 mm high. The load is applied through two loading cylinders spaced 90 mm apart, while the supports are positioned at a distance of 270 mm. This testing configuration is employed to investigate the flexural response of beams for different filament orientations with respect to the loading direction. The three loading configurations examined in this study are illustrated in Fig. 31. In the numerical models, a uniform vertical displacement of 0.5 mm is applied at the load transmission points defined in the experimental setup. One of the two support points is fully constrained in all translational degrees of freedom ($U_x = U_y = U_z$), while the other support is allowed to move freely in the horizontal direction to prevent spurious constraint effects.

The resulting load–deflection curves are shown in Fig. 32, where the applied load is plotted against the midspan deflection of the beam.

Since experimental load–deflection data are not available for this study, the comparison is carried out in terms of peak flexural stress, calculated according to ASTM C78 [47], which was followed in the experimental campaign, that is: $\sigma_f = \frac{F_f L}{bd^2}$, where σ_f is the flexural (cracking) stress, F_f is the measured peak load, L the span length, and b and d are the specimen width and depth, respectively.

The results show that the anisotropic mechanical response of the material is consistently captured by the numerical model in terms of flexural strength. The lowest flexural strength is observed in direction F_x, in agreement with the trends reported in Section 3.3 for the four-point bending tests conducted on Material 2. This direction exhibits the most brittle behavior, as bending induces tensile stresses perpendicular to the interfaces, leading to failure by tension and separation along the interlayer boundaries. Conversely, in directions F_y and F_z, the flexural strengths are comparable to those obtained for the homogeneous (cast) specimen.

Fig. 33 shows the distributions of normal and shear stresses at peak load for all three loading directions, together with the corresponding tensile damage contours.

In direction X, tensile decohesion localizes along the T-interfaces (Fig. 33(b)), confirming that this is the dominant failure mechanism when interfaces are parallel to the loading direction. Tensile damage develops only at the final stage of the analysis and propagates from the opening that forms between adjacent interfaces (Fig. 33(c)).

In contrast, in directions Y and Z the interfaces are primarily subjected to shear stresses induced by interlayer sliding, while failure occurs when the tensile strength of the concrete is exceeded. In both cases — along T-interfaces in direction Y (Fig. 33(d)) and D-interfaces in direction Z (Fig. 33(g)) — the maximum shear stress remains below the critical value, indicating a limited contribution of the interfaces to the overall flexural strength. This explains why the flexural strength in directions Y and Z closely matches that of the homogeneous specimen and why the presence of interfaces does not significantly influence the ultimate load.

The numerically predicted failure mode in direction X is in excellent agreement with the experimental observations reported in [19]. In directions Y and Z, failure localizes along only one of the two potential crack paths identified numerically. Nevertheless, the overall agreement is satisfactory, demonstrating that the proposed numerical models can accurately reproduce the experimental behavior.

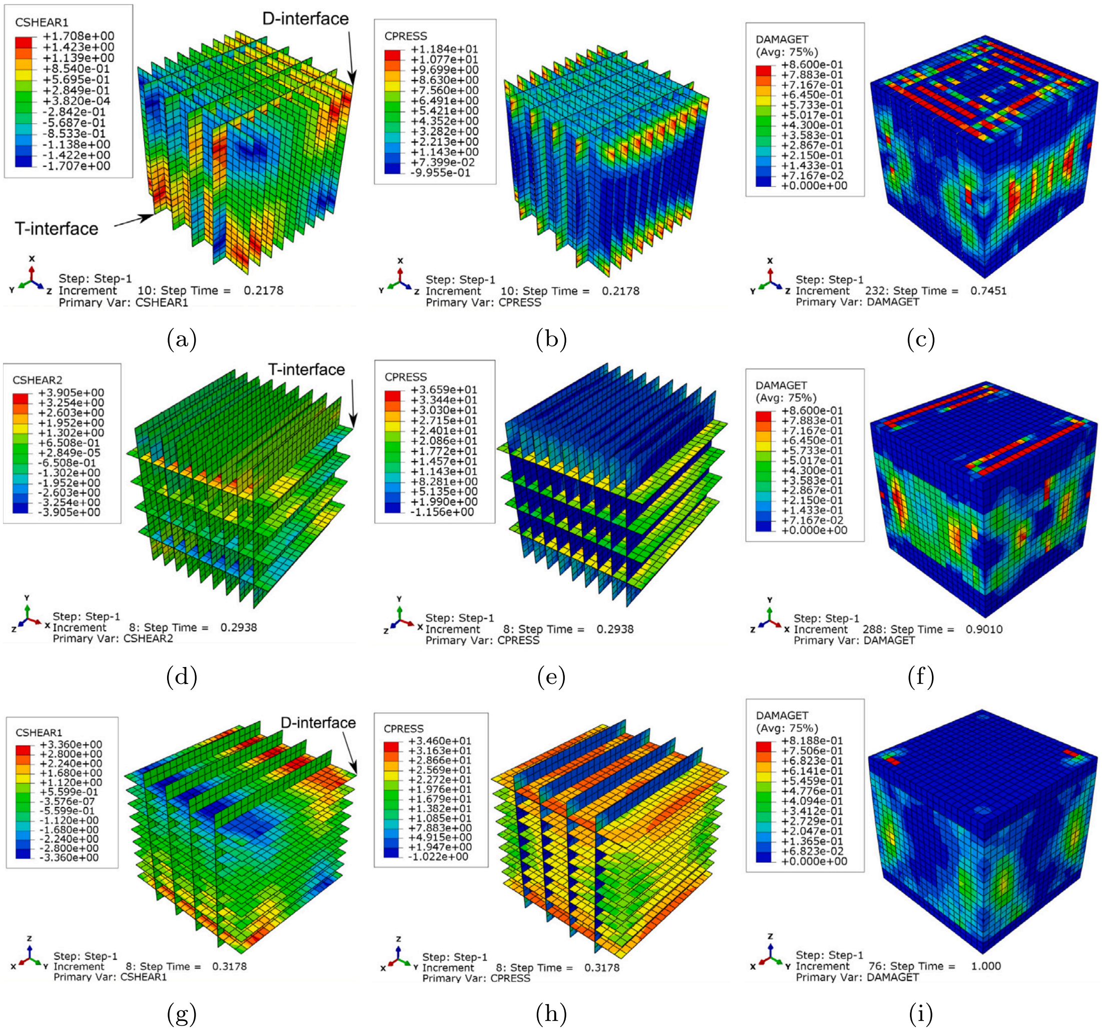

Fig. 30. Material 3: numerical results of the compression test with loading along X (a–c), Y (d–f), and Z (g–i): maximum shear stress distribution along the interfaces; maximum interface pressure distribution; tensile damage at failure.

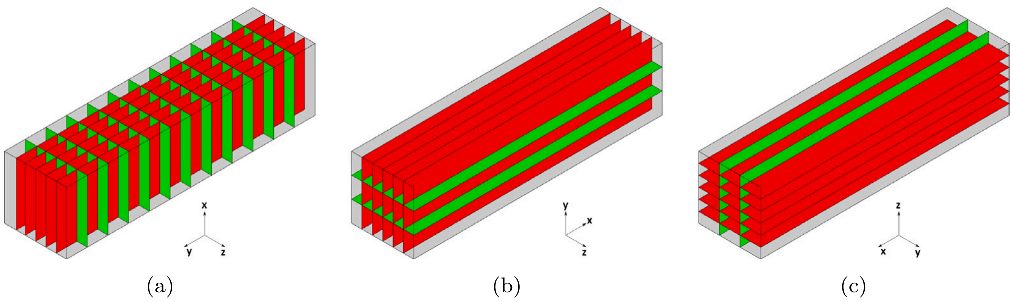

Fig. 31. Four-point bending test loading directions: X (a), Y (b), and Z (c).

A parametric study is finally conducted to assess the influence of interface properties on the flexural strength. Four scaling factors — 0.25, 0.5, 1.0, and 2.0 — are applied to the cohesive strengths f_p and f_s. The results reported in [19] show that reducing the cohesive strengths leads to a nearly proportional decrease in flexural capacity.

In direction X, the flexural response is primarily governed by the tensile strength of the T-interfaces, as evidenced by the normal stress distributions shown in Fig. 34(a)–Fig. 34(c). For scaling factors of 0.25 and 0.5, the peak load is reached when the interface

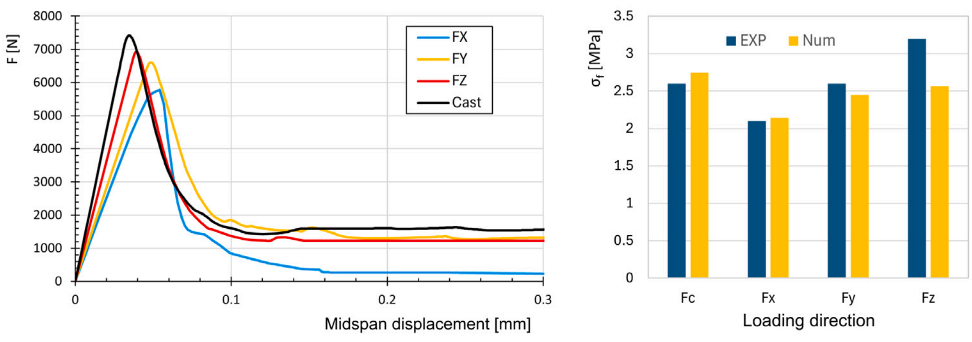

(a) (b)

Fig. 32. Material 3: results of the four-point bending tests (a) and comparison with experimental flexural strengths (b).

Table 3
Quantitative validation of the proposed cohesive contact model against experimental results.

Material	Test	Experimental Peak load	Numerical Peak load	Relative error (%)	Experimental Peak disp./CMOD	Numerical Peak disp./CMOD	Relative error (%)
1 (HP)	Direct tension	1214 N	1192 N	1.8	0.00194 mm	0.00220 mm	13.4
1 (HP)	Iosipescu shear	1775 N	1682 N	5.2	0.070 mm	0.066 mm	5.7
2 (FR)	Direct tension (D1)	2113 N	2414 N	14.3	0.0064 mm	0.0073 mm	14.1
2 (FR)	Direct tension (D3)	1007 N	1106 N	9.8	0.0032 mm (CMOD)	0.0034 mm (CMOD)	6.3
2 (FR)	4-point bending (D1)	982 N	913 N	7.0	NR	NR	NR
2 (FR)	4-point bending (D3)	444 N	427 N	3.8	Force–CMOD curve	Force–CMOD curve	Good agreement
3 (NS)	Compression	NR	NR	NR	NR	NR	NR
3 (NS)	4-point bending	NR	NR	NR	NR	NR	NR

HP = High-performance concrete; FR = Fiber-reinforced concrete; NS = Natural sand concrete.
NR = Not reported in the original experimental study.
For the four-point bending test in the D3 direction, only the agreement of the complete force–CMOD response is reported, since peak CMOD values are not explicitly available.

tensile stress attains the corresponding limits $0.25f_p$ and $0.5f_p$. In contrast, for the case $2f_p$ (Fig. 34(c)), the interfacial tensile strength exceeds that of the concrete, and the failure mode becomes comparable to that of the homogeneous specimen.

In direction Y, a reduction in the shear strength f_s of the T-interfaces results in a clear decrease in flexural strength, with lower values of f_s causing earlier failure in shear-dominated regions (Fig. 34(d) and Fig. 34(e)). For $f_s = 1.0f_s$ and $2.0f_s$, the interface shear strength no longer governs the response, as it exceeds the maximum shear stress attained in the simulations. A similar behavior is observed in direction Z (Fig. 34(g)-Fig. 34(i)), where in this case the D-interfaces dominate the shear failure mechanism.

These results confirm that interface properties play a critical role in controlling the flexural response of 3DPC when the failure mode is interface-driven.

4. Discussion

The proposed cohesive contact formulation was validated against a series of experimental case studies involving direct tension, shear, compression, and four-point bending tests on three different 3D-printed concrete materials. A quantitative comparison between the experimental and numerical responses is summarized in Table 3.

For the case studies where numerical values are available, the proposed model accurately predicts the peak load. In particular, the direct tensile test performed on the high-performance concrete (Material 1) exhibits a numerical peak load of 1192 N compared with the experimental value of 1214 N, corresponding to a relative error of only 1.8%. Similarly, the Iosipescu shear test yields a peak load of 1682 N compared with the measured value of 1775 N, resulting in a relative error of 5.2%. The predicted peak displacements also show satisfactory agreement with the experiments, with relative errors of 13.4% for the direct tensile test and 5.7% for the shear test. These results demonstrate that the proposed cohesive contact formulation provides an accurate prediction of the onset of interface failure under both tensile and shear loading conditions.

For the fiber-reinforced concrete (Material 2), both force–displacement and force–CMOD responses are reproduced with good accuracy. In the direct tensile test along the D1 direction, failure occurs in the bulk concrete, and the numerical model predicts a peak load of 2414 N compared with the experimental value of 2113 N, corresponding to a difference of approximately 14%. The corresponding peak displacement is 0.0073 mm, compared with the experimental value of 0.0064 mm.

Particular attention should be paid to the direct tensile test in the D3 direction, where failure is governed by the interlayer interfaces and the response is reported in terms of force–CMOD curves. The proposed model predicts a maximum load of 1106 N

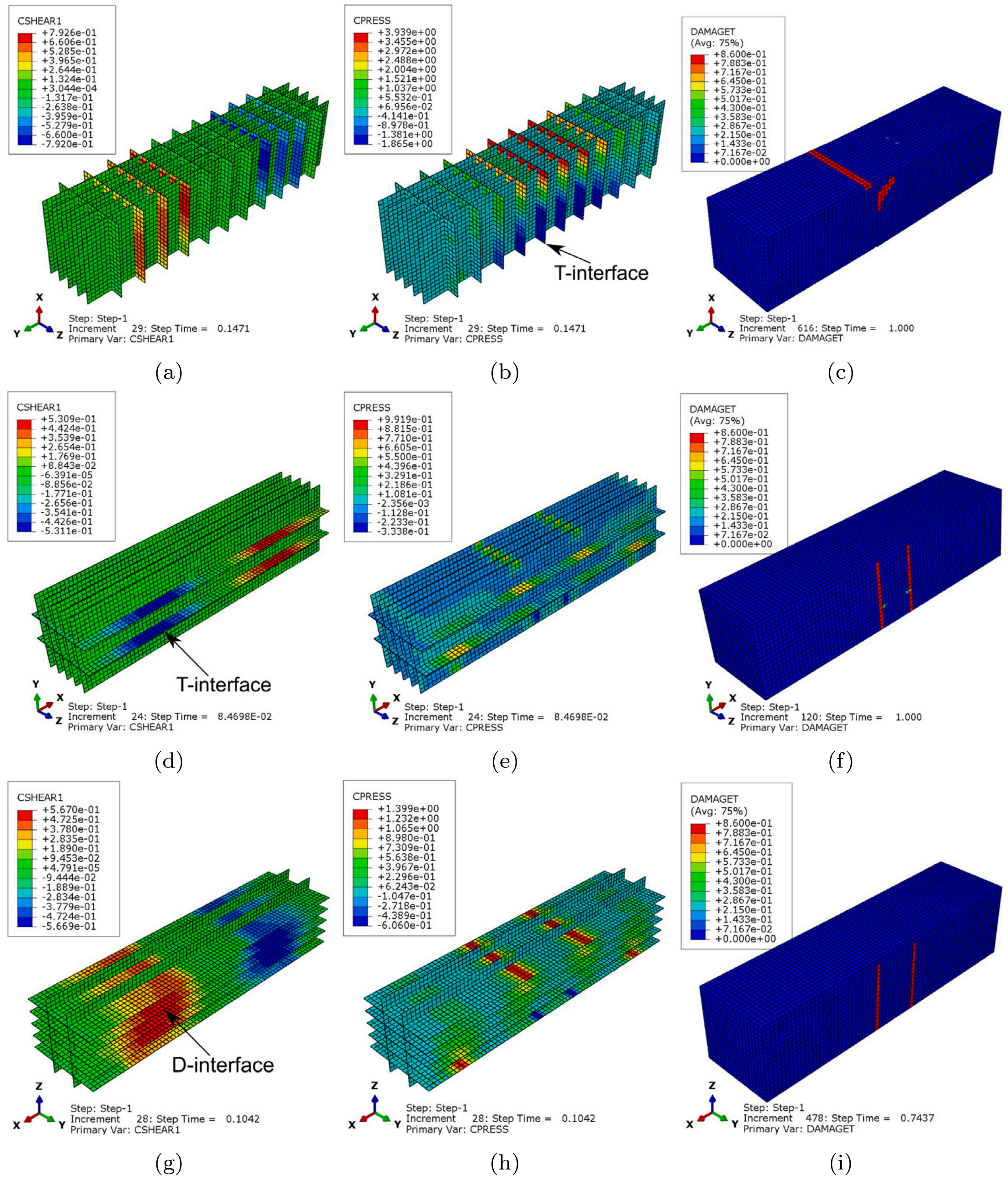

Fig. 33. Material 3: numerical results of the four-point bending test with loading along X (a–c), Y (d–f), and Z (g–i): maximum shear stress distribution along the interfaces; maximum interface pressure distribution; tensile damage at failure.

compared with the experimental value of 1007 N, corresponding to a relative error of 9.8%. More importantly, the CMOD at peak load is predicted as 0.0034 mm, compared with the experimental value of 0.0032 mm, corresponding to a relative error of only 6.3%. Moreover, the numerical model successfully reproduces the entire post-peak softening branch, extending from a CMOD of approximately 0.0032 mm to about 0.43 mm, thereby accurately describing the progressive degradation of the interlayer bond after crack initiation.

The proposed model also provides an accurate description of the flexural behavior. For the four-point bending tests on Material 2, the numerical peak load in the D1 direction is 913 N, compared with the experimental value of 982 N, resulting in a deviation of approximately 7%. In the D3 direction, where the structural response is governed by interface decohesion, the numerical and experimental peak loads are 427 N and 444 N, respectively, corresponding to a relative error of only 3.8%. Furthermore, the

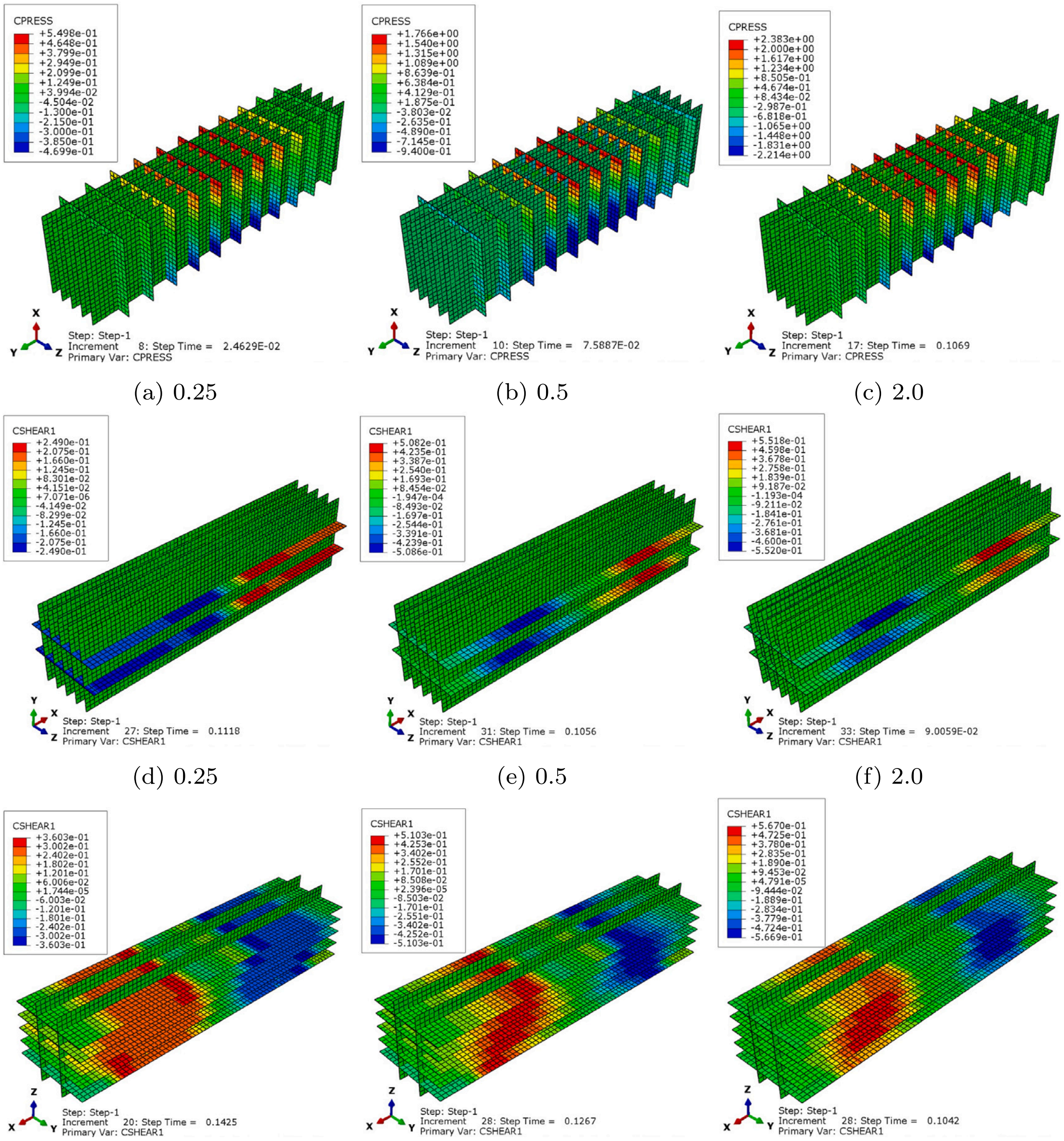

(a) 0.25 (b) 0.5 (c) 2.0

(d) 0.25 (e) 0.5 (f) 2.0

(g) 0.25 (h) 0.5 (i) 2.0

Fig. 34. Material 3: influence of interface parameters on the maximum interface pressure distribution and maximum shear stress distribution along the interfaces in the four-point bending test with loading along X (a–c), Y (d–f), and Z (g–i).

numerical force–CMOD curves correctly reproduce the experimentally observed exponential post-peak softening, confirming the capability of the cohesive formulation to capture fracture energy dissipation during interface separation.

Beyond the prediction of peak strength, the numerical simulations reproduce the global mechanical response observed experimentally. In all investigated cases, the initial elastic stiffness is accurately captured, indicating that the adopted interface stiffness parameters provide a consistent representation of the interlayer interaction before damage initiation. The post-peak response is also satisfactorily reproduced through the proposed hardening/softening formulation. For the direct tensile tests, the calibrated softening law successfully describes the progressive degradation of the interface after peak load, while in the Iosipescu shear tests the simulations correctly predict the abrupt brittle failure associated with complete interface separation.

For the validation cases reported in terms of force–CMOD curves, the proposed model also provides a satisfactory prediction of the crack mouth opening displacement throughout the loading process. Although complete numerical values of the peak CMOD are not available for all experimental studies, the comparison of the experimental and numerical force–CMOD curves shows that the proposed cohesive formulation accurately reproduces both the onset and the subsequent evolution of crack opening. This agreement is particularly significant because CMOD directly reflects the progressive degradation of the interlayer interface and is therefore highly sensitive to the adopted traction–separation law.

The proposed model also reproduces the experimentally observed failure mechanisms. In the direct tensile tests, failure is correctly predicted as localized tensile fracture at the central interlayer interface, where the normal interface strength is first reached. Likewise, the numerical simulations of the Iosipescu tests accurately reproduce the localization of shear stresses at the central interface and the subsequent separation of the specimen into two distinct parts. For the remaining validation examples, including four-point bending and compression tests, the simulations correctly capture the dominant failure mechanisms reported experimentally, namely interface-controlled flexural cracking and compressive crushing.

Overall, the proposed cohesive contact model accurately reproduces the global mechanical response observed in the experiments. Peak-load errors remain below approximately 10% for most interface-dominated problems and below 7% for the bending validation cases, while the CMOD evolution and post-peak softening are also captured with good accuracy. Further, the model correctly predicts the governing failure mechanisms, including interface tensile fracture, interface shear failure, compressive crushing, and flexural cracking along the interlayer interfaces, demonstrating its capability to reproduce both the global response and the local failure processes of layered concrete structures.

5. Conclusions

This work presents a comprehensive numerical framework for the mechanical characterization of 3D-printed concrete, explicitly accounting for the role of interlayer interfaces through a cohesive contact formulation. The proposed model combines the Concrete Damage Plasticity approach for the bulk material with an elasto-plastic cohesive zone model for interfaces, implemented in Abaqus via a user-defined contact subroutine. The formulation captures the coupled normal–tangential response of interfaces and allows for the description of hardening, softening, and residual strength effects.

The numerical framework is validated against three independent experimental campaigns involving different materials, printing configurations, and testing methodologies.

When experimental force–displacement curves from direct tensile and shear tests are available, the cohesive traction–separation laws can be accurately calibrated to reproduce the observed interfacial response. Once calibrated, the same interface formulation yields reliable predictions for structurally more complex loading conditions, such as four-point bending, without requiring any additional parameter tuning. In this regard, the numerical results obtained for Materials 1 and 2 demonstrate the consistency, robustness, and transferability of the proposed cohesive interface model across different loading configurations.

In the absence of experimental interface data, the proposed modeling framework can be extended by adopting interface properties derived from design standards and established formulations in the literature. Although this approach necessarily introduces additional assumptions, the numerical simulations performed for Material 3 are still able to capture the experimentally observed anisotropic mechanical behavior, particularly under compressive and flexural loading. This confirms the applicability of the proposed methodology also in situations where direct interface characterization is not available.

Overall, good agreement is achieved between numerical and experimental results in terms of peak loads, force–displacement (or force–CMOD) curves, and observed failure modes for direct tensile, shear, compression, and four-point bending tests.

The results demonstrate that the proposed cohesive contact model accurately reproduces the experimentally observed post-peak response for those case studies in which complete softening data are available. For the remaining validation cases, the model is shown to reliably predict the peak strength and the governing failure mechanism, whether controlled by interlayer decohesion or by damage initiation within the concrete matrix.

The simulations confirm the strongly anisotropic mechanical behavior of 3D-printed concrete. In tension and bending, the structural response is governed either by the tensile strength of the bulk concrete or by the cohesive strength of the interfaces, depending on whether the interfaces are oriented parallel or orthogonal to the loading direction. Under compressive loading, failure is predominantly controlled by interfacial shear resulting from transverse expansion, emphasizing the critical role of interface sliding — particularly along transition interfaces (T-interfaces) — in determining the compressive response.

A parametric analysis further demonstrates that the cohesive strengths of the interfaces have a direct and proportional influence on flexural capacity when failure is interface-driven. When the interfacial strength exceeds that of the bulk material, the mechanical response approaches that of a homogeneous specimen. Conversely, weaker interfaces promote early decohesion and a marked reduction in load-bearing capacity. These findings highlight the central role of interface properties in governing the structural performance of 3D-printed concrete elements.

In conclusion, the proposed cohesive contact formulation provides a robust and versatile framework for the numerical simulation of 3D-printed concrete structures. The validation against different experimental campaigns demonstrates that the model accurately reproduces not only the peak strengths but also the force–displacement (or force–CMOD) responses, post-peak softening behavior, and the governing failure mechanisms under direct tension, shear, compression, and four-point bending. The coupled normal–tangential constitutive formulation further enables the realistic simulation of mixed-mode interface failure, making the proposed approach suitable for the analysis of complex loading conditions commonly encountered in layered concrete structures.

The applicability of the proposed methodology is primarily limited by the extent to which the adopted effective interface constitutive law can represent the mechanical response observed under the loading conditions of interest. Although the model parameters can be identified from experimental interface tests, their transferability across different printing configurations, material batches, curing conditions, and loading paths cannot be assumed a priori. In particular, different combinations of stiffness, strength, and hardening/softening parameters may reproduce a similar global response while leading to different predictions of damage initiation, localization, and post-peak dissipation. The identified parameters should therefore be regarded as effective quantities associated with a specific experimental and manufacturing context rather than as intrinsic material constants. Moreover, the proposed formulation does not explicitly resolve microstructural features such as pore distribution, local defects, surface roughness, moisture gradients, or other printing-induced imperfections. Their combined influence is represented only implicitly through the effective interface response, which may reduce the predictive capability of the model when applied outside the range of conditions used for its identification.

Finally, in the absence of independent evidence supporting distinct constitutive descriptions, the deposition (D-) and transition (T-) interfaces were assigned the same effective mechanical properties. This assumption was sufficient for the validation cases considered here, but it should not be interpreted as implying mechanical equivalence between the two interface types. Its adequacy depends on the extent to which differences arising from the local deposition history, filament arrangement, surface morphology, and loading orientation affect the structural response. Accordingly, the present formulation is most reliable when such differences have a secondary influence at the scale of interest. In configurations where D- and T-interfaces govern different failure mechanisms, separate constitutive descriptions may be required. The current model also represents the printed filaments as isotropic continua and adopts a simplified treatment of interface behavior under combined compression and shear; therefore, effects associated with filament anisotropy, frictional contact, and aggregate interlock are included only through the effective calibrated response.

CRediT authorship contribution statement

Gianluca Mazzucco: Writing – original draft, Validation, Supervision, Methodology, Conceptualization. **Massimiliano Maletta:** Writing – original draft, Formal analysis. **Riccardo Lando:** Writing – review & editing, Formal analysis, Data curation. **Jiangkun Zhang:** Writing – review & editing, Data curation. **Valentina Salomoni:** Writing – review & editing. **Beatrice Pomaro:** Writing – review & editing, Project administration, Data curation.

Declaration of competing interest

The authors declare that they have no known competing financial interests or personal relationships that could have appeared to influence the work reported in this paper.

Acknowledgments

The financial support from the Italian Ministry of University and Research (MUR) in the framework of PRIN2022 PNRR Project P2022BTAPP is gratefully acknowledged.

Data availability

Data will be made available on request.

References

[1] Flatt RJ, Roussel N, Cheeseman CR. Concrete: An eco material that needs to be improved. J Eur Ceram Soc 2012;32(11):2787–98. http://dx.doi.org/10.1016/j.jeurceramsoc.2011.11.012, Special Issue: ECerS XII, 12th Conference of the European Ceramic Society.

[2] Freek Bos ZA, Salet T. Additive manufacturing of concrete in construction: potentials and challenges of 3D concrete printing. Virtual Phys Prototyp 2016;11(3):209–25. http://dx.doi.org/10.1080/17452759.2016.1209867.

[3] Panda B, Paul SC, Mohamed NAN, Tay YWD, Tan MJ. Measurement of tensile bond strength of 3D printed geopolymer mortar. Measurement 2018;113:108–16. http://dx.doi.org/10.1016/j.measurement.2017.08.051.

[4] van den Heever M, du Plessis A, Kruger J, van Zijl G. Evaluating the effects of porosity on the mechanical properties of extrusion-based 3D printed concrete. Cem Concr Res 2022;153:106695. http://dx.doi.org/10.1016/j.cemconres.2021.106695.

[5] Xiao J, Liu H, Ding T. Finite element analysis on the anisotropic behavior of 3D printed concrete under compression and flexure. Addit Manuf 2021;39:101712. http://dx.doi.org/10.1016/j.addma.2020.101712.

[6] Liu H, Xiao J, Ding T. Flexural performance of 3D-printed composite beams with ECC and recycled fine aggregate concrete: Experimental and numerical analysis. Eng Struct 2023;283:115865. http://dx.doi.org/10.1016/j.engstruct.2023.115865.

[7] Ye J, Yang M, Yu J, Dai Y, Yin B, Weng Y. Size effect on flexural and fracture behaviors of 3D printed engineered cementitious composites: Experimental and numerical studies. Eng Struct 2024;298:117062. http://dx.doi.org/10.1016/j.engstruct.2023.117062.

[8] van den Heever M, Bester F, Pourbehi M, Kruger J, Cho S, van Zijl G. Characterizing the fissility of 3D concrete printed elements via the cohesive zone method. In: Bos FP, Lucas SS, Wolfs RJ, Salet TA, editors. Second RILEM international conference on concrete and digital fabrication. Cham, Switzerland: Springer International Publishing; 2020, p. 489–99.

[9] Camanho PP, Davila C, De Moura M. Numerical simulation of mixed-mode progressive delamination in composite materials. J Compos Mater 2003;37(16):1415–38. http://dx.doi.org/10.1177/0021998303034505.

[10] Le T, Austin S, Lim S, Buswell R, Law R, Gibb A, Thorpe T. Hardened properties of high-performance printing concrete. Cem Concr Res 2012;42(3):558–66. http://dx.doi.org/10.1016/j.cemconres.2011.12.003.

[11] van den Heever M, Bester F, Kruger J, van Zijl G. Mechanical characterisation for numerical simulation of extrusion-based 3D concrete printing. J Build Eng 2021;44:102944. http://dx.doi.org/10.1016/j.jobe.2021.102944.

[12] Ma G, Li Z, Wang L. Printable properties of cementitious material containing copper tailings for extrusion based 3D printing. Constr Build Mater 2018;162:613–27. http://dx.doi.org/10.1016/j.conbuildmat.2017.12.051.

[13] Wang L, Tian Z, Ma G, Zhang M. Interlayer bonding improvement of 3D printed concrete with polymer modified mortar: Experiments and molecular dynamics studies. Cem Concr Compos 2020;110:103571. http://dx.doi.org/10.1016/j.cemconcomp.2020.103571.

[14] Feng P, Meng X, Chen J-F, Ye L. Mechanical properties of structures 3D printed with cementitious powders. Constr Build Mater 2015;93:486–97. http://dx.doi.org/10.1016/j.conbuildmat.2015.05.132.

[15] Le TT, Austin SA, Lim S, Buswell RA, Gibb AG, Thorpe T. Mix design and fresh properties for high-performance printing concrete. Mater Struct 2012;45:1221–32. http://dx.doi.org/10.1617/s11527-012-9828-z.

[16] Ma G, Li Z, Wang L, Wang F, Sanjayan J. Mechanical anisotropy of aligned fiber reinforced composite for extrusion-based 3D printing. Constr Build Mater 2019;202:770–83. http://dx.doi.org/10.1016/j.conbuildmat.2019.01.008.

[17] Wolfs R, Bos F, Salet T. Hardened properties of 3D printed concrete: The influence of process parameters on interlayer adhesion. Cem Concr Res 2019;119:132–40. http://dx.doi.org/10.1016/j.cemconres.2019.02.017.

[18] Rahul A, Santhanam M, Meena H, Ghani Z. Mechanical characterization of 3D printable concrete. Constr Build Mater 2019;227:116710. http://dx.doi.org/10.1016/j.conbuildmat.2019.116710.

[19] Ding T, Xiao J, Zou S, Wang Y. Hardened properties of layered 3D printed concrete with recycled sand. Cem Concr Compos 2020;113:103724. http://dx.doi.org/10.1016/j.cemconcomp.2020.103724.

[20] Li Z, Hojati M, Wu Z, Piasente J, Ashrafi N, Duarte JP, Nazarian S, Bilén SG, Memari AM, Radlińska A. Fresh and hardened properties of extrusion-based 3D-printed cementitious materials: A review. Sustainability 2020;12(14):5628. http://dx.doi.org/10.3390/su12145628.

[21] Panda B, Chandra Paul S, Jen Tan M. Anisotropic mechanical performance of 3D printed fiber reinforced sustainable construction material. Mater Lett 2017;209:146–9. http://dx.doi.org/10.1016/j.matlet.2017.07.123.

[22] Sanjayan JG, Nematollahi B, Xia M, Marchment T. Effect of surface moisture on inter-layer strength of 3D printed concrete. Constr Build Mater 2018;172:468–75. http://dx.doi.org/10.1016/j.conbuildmat.2018.03.232.

[23] Hambach M, Volkmer D. Properties of 3D-printed fiber-reinforced portland cement paste. Cem Concr Compos 2017;79:62–70. http://dx.doi.org/10.1016/j.cemconcomp.2017.02.001.

[24] Nematollahi B, Vijay P, Sanjayan J, Nazari A, Xia M, Naidu Nerella V, Mechtcherine V. Effect of polypropylene fibre addition on properties of geopolymers made by 3D printing for digital construction. Materials 2018;11(12):2352. http://dx.doi.org/10.3390/ma11122352.

[25] Zhang Y, Zhang Y, She W, Yang L, Liu G, Yang Y. Rheological and harden properties of the high-thixotropy 3D printing concrete. Constr Build Mater 2019;201:278–85. http://dx.doi.org/10.1016/j.conbuildmat.2018.12.061.

[26] Paul SC, Tay YWD, Panda B, Tan MJ. Fresh and hardened properties of 3D printable cementitious materials for building and construction. Arch Civ Mech Eng 2018;18(1):311–9. http://dx.doi.org/10.1016/j.acme.2017.02.008.

[27] Soltan DG, Li VC. A self-reinforced cementitious composite for building-scale 3D printing. Cem Concr Compos 2018;90:1–13. http://dx.doi.org/10.1016/j.cemconcomp.2018.03.017.

[28] Wang H, Shao J, Zhang J, Zou D, Sun X. Bond shear performances and constitutive model of interfaces between vertical and horizontal filaments of 3D printed concrete. Constr Build Mater 2022;316:125819. http://dx.doi.org/10.1016/j.conbuildmat.2021.125819.

[29] Napolitano R, Forni D, Menna C, Asprone D, Cadoni E. Dynamic characterization of the layer-interface properties of 3D-printed concrete elements. Case Stud Constr Mater 2021;15:e00780. http://dx.doi.org/10.1016/j.cscm.2021.e00780.

[30] Meurer M, Classen M. Mechanical properties of hardened 3D printed concretes and mortars: Development of a consistent experimental characterization strategy. Materials 2021;14(4):752. http://dx.doi.org/10.3390/ma14040752.

[31] Yao H, Xie Z, Li Z, Huang C, Yuan Q, Zheng X. The relationship between the rheological behavior and interlayer bonding properties of 3D printing cementitious materials with the addition of attapulgite. Constr Build Mater 2022;316:125809. http://dx.doi.org/10.1016/j.conbuildmat.2021.125809.

[32] Wang L, Liu Y, Yang Y, Li Y, Bai M. Bonding performance of 3D printing concrete with self-locking interfaces exposed to compression–shear and compression–splitting stresses. Addit Manuf 2021;42:101992. http://dx.doi.org/10.1016/j.addma.2021.101992.

[33] Classen M, Adam V, Hillebrand M. Torsion test setup to investigate aggregate interlock and mixed mode fracture of monolithic and 3D-printed concrete. In: Fib symposium. 2019, p. 521–8.

[34] Becks H, Schmidt M, Bosbach S, Classen M. Large-scale combined torsional and axial loading system (TorAx) – A new perspective on multiaxial testing of fracture and stress transfer in plain and reinforced concrete. Eng Struct 2024;302:117391. http://dx.doi.org/10.1016/j.engstruct.2023.117391.

[35] Simulia. Dassault systèmes. abaqus 2025 User Manual. 2025.

[36] Barenblatt GI. The mathematical theory of equilibrium cracks in brittle fracture. Adv Appl Mech 1962;7:55–129.

[37] Kaliyavaradhan SK, Ambily P, Prem PR, Ghodke SB. Test methods for 3D printable concrete. Autom Constr 2022;142:104529. http://dx.doi.org/10.1016/j.autcon.2022.104529.

[38] Wriggers P, Laursen TA. In: Computational contact mechanics, vol. 2, Springer; 2006.

[39] Fib. Fib model code for concrete structures 2010. Lausanne: John Wiley & Sons; 2013.

[40] American Concrete Institute. Building code requirements for structural concrete (ACI 318-05) and commentary (ACI 318R-05). Farmington Hills, MI: American Concrete Institute; 2005.

[41] Lubliner J, Oliver J, Oller S, Oñate E. A plastic-damage model for concrete. Int J Solids Struct 1989;25(3):299–326. http://dx.doi.org/10.1016/0020-7683(89)90050-4.

[42] Lee J, Fenves GL. Plastic-damage model for cyclic loading of concrete structures. J Eng Mech 1998;124(8):892–900. http://dx.doi.org/10.1061/(ASCE)0733-9399(1998)124:8(892).

[43] Desayi P, Krishnan S. Discussion of "equation for the stress–strain curve of concrete" by desayi and krishnan. J Am Concr Inst 1964;61:1229–35.

[44] Hordijk DA. Local approach to fatigue of concrete [Ph.D. thesis], Delft, The Netherlands: Delft University of Technology; 1991.

[45] He L, Chow WT, Li H. Effects of interlayer notch and shear stress on interlayer strength of 3D printed cement paste. Addit Manuf 2020;36:101390. http://dx.doi.org/10.1016/j.addma.2020.101390.

[46] Wu JY, Li J, Faria R. An energy release rate-based plastic-damage model for concrete. Int J Solids Struct 2006;43(3):583–612. http://dx.doi.org/10.1016/j.ijsolstr.2005.05.038.

[47] ASTM International Committee C09 on Concrete and Concrete Aggregates (ASTM C293/C293M). Standard test method for flexural strength of concrete (using simple beam with center-point loading). West Conshohocken, PA: ASTM International; 2016.